UNIVERSITÀ
DEGLI STUDI
FIRENZE

SCUOLA DI SCIENZE MATEMATICHE FISICHE E NATURALI

Corso di Laurea Magistrale in Scienze Fisiche e Astrofisiche

Sviluppo di una nuova piattaforma per simulazione quantistica con atomi Rydberg di Sr

Development of a novel platform for quantum simulation with Sr Rydberg atoms

Relatore:
Prof. Leonardo Fallani

Candidato:
Veronica Giardini

Relatore esterno:
Dr. Giacomo Cappellini

Anno Accademico 2020-2021

Ad Alessia, Fosco e Pietro.

Contents

1 Introduction on quantum simulation **4**

2 Strontium Rydberg atoms **6**

2.1 Strontium 6

2.2 Excitation towards the Rydberg state 9

2.3 Rydberg blockade mechanism 10

2.4 Rydberg atoms in optical tweezers 12

3 Cooling and trapping **17**

3.1 Deceleration of an atomic beam 17

3.2 Zeeman slower 18

3.3 Doppler cooling 20

3.4 Magneto-Optical Trap 23

4 Overview on the experimental setup **26**

4.1 The atomic source 26

4.2 Experimental sequence 29

4.3 The glass cell 29

5 Design of the high-field coils **32**

5.1 Magnetic field simulation 35

5.2 Cooling simulation 42

5.2.1 Water flow in the coils 43

5.2.2 Heat exchange 45

5.2.3 Results 47

6 Measurements and results **54**
6.1 Blue laser 54
6.2 Spectroscopy measurements 59
6.2.1 Calibration 60
6.2.2 Spectroscopy near the oven 62
6.2.3 Spectroscopy near the hot window 64
6.2.4 Error signal 66
6.3 Red laser 68
6.3.1 Pound-Drever-Hall 73

7 Conclusions and perspectives **78**

Chapter 1

Introduction on quantum simulation

The greatest difficulty in the direct simulation of quantum phenomena on classical computers is the huge amount of memory required to store the explicit state of a quantum system. The number of parameters needed to describe these states and the number of operation required to simulate the evolution of these systems grow exponentially with the size of the system itself [1]. Richard Feynman in 1982 was the first to think of using quantum mechanical devices to efficiently simulate quantum systems [2]. The alternative approach he suggested is to have "one controllable quantum system simulate another". The approach introduced by Feynman is usually referred to as quantum simulation. Quantum simulators are controllable quantum systems that can be used to simulate other systems allowing for the study of a wide range of complex physical phenomena. These quantum devices exploit entanglement and many-particle behavior to explore and solve hard scientific, and computational problems. Moreover, being their hardware intrinsically quantum, these simulators are best suited to tackle problems of quantum physics that are unmanageable or time-prohibitive on classical computers, and those for which more direct studies are very difficult or impossible. These devices grant indeed a high degree of controllability over the parameters of the physical system under investigation [3]. In the last twenty years such machines have been constructed using a variety of quantum architectures, such as photons [4], trapped ions [5], degenerate quantum gases in optical lattices [6] and quantum dot systems [7].

This thesis is focused on a new kind of platform for quantum simulation based on individual Rydberg atoms trapped in an array of optical "tweezers" (micron-scale optical traps obtained by tightly focusing individual laser beams) with fully

programmable geometry and zero configurational entropy. With this platform it is possible to combine the high degree of quantum control and fast experimental cycles as it happens with trapped ions platforms with the versatility of a completely optical trapping technique, which allows the number of particles to be upscaled more easily than in the case of trapped ions, up to hundreds of particles. Furthermore it is possible to have high control over single atoms, that is challenging in quantum gases in optical lattice.

Exploiting advanced optical techniques which include the use of Spatial Light Modulators (SLMs) and Acusto-Optic Deflectors (AODs), driven by a radio-frequency (RF) signal, it is possible to realize defect-free arrays of atoms with arbitrary geometry, that allow for the realization of quantum simulators with different topologies, that can be probed via high-fidelity imaging with single-atom resolution performed through the same high-resolution objective that is used to generate the optical tweezers.

The excitation of the atoms towards the Rydberg states (states with high principal quantum number), that can induce strong "tunable" long-range interactions, is employed to control the interaction between the atoms in the array, allowing for the creation of very robust entangled states which can be exploited to implement state-of-the-art quantum simulations schemes [8].

In this thesis I worked on the development of the first Italian platform with Rydberg atoms in optical tweezers, that will exploit alkaline-heart strontium atoms. In particular I designed the high-field coil, for the MOT (Magneto Optical Trap) and for the excitation of the clock transition, performing simulations both on the magnetic field generated as a function of the wire and coil geometry and on the cooling system to ensure correct operation, exploiting the COMSOL multiphysics software.

I also characterized two laser sources, the 461 nm blue laser that is used both for the generation of the first MOT stage and for the detection fluorescence scheme, and the 689 nm red laser for the realization of the second and cooler MOT stage and for the two-photon Rydberg excitation scheme. Finally I performed some preliminary spectroscopy measurement towards characterizing the atomic beam emitted from the source.

Chapter 2

Strontium Rydberg atoms

2.1 Strontium

Most of the experiments made with Rydberg atoms in optical tweezers use alkaline atoms such as Rubidium [9, 10, 11], but in recent years, experiments that exploit alkaline-earth atoms have been realized too [12, 13]. Alkaline-earth atoms have two valence electrons, unlike alkalis that just have one. The spins of these electrons can be aligned anti-parallel (singlet states, $S = 0$) or parallel (triplet states, $S = 1$). This present many advantages mainly because of the richness of their energy level structure.

Strontium (Sr) is an alkaline-earth atom of atomic number $Z = 38$, in the ground state it has an electronic configuration $[\mathrm{Kr}]5s^2$. Strontium occurs in nature with 4 different isotopes, which are listed together with their properties in table 2.1.

Isotope	Natural abundance	Statistics	Nuclear spin
^{84}Sr	0.56 %	bosonic	0
^{86}Sr	9.86 %	bosonic	0
^{87}Sr	7 %	fermionic	$\frac{9}{2}$
^{88}Sr	82.58 %	bosonic	0

Table 2.1: Properties of stables isotopes of strontium, data taken from [14].

The most common one is a boson, ^{88}Sr, with abundance of approximately 82.6%. There are two other bosons, ^{86}Sr and ^{84}Sr, with abundance 9.86% and 0.56%, respectively, and a fermionic isotope ^{87}Sr with a rather large nuclear spin of $I = 9/2$ and with abundance 7%. All the boson isotopes have $I = 0$, resulting in a lack

of hyperfine structure [14]. A diagram showing the lowest-lying singlet and triplet states, with some relevant optical transition, for a Strontium atom is reported in figure 2.1.

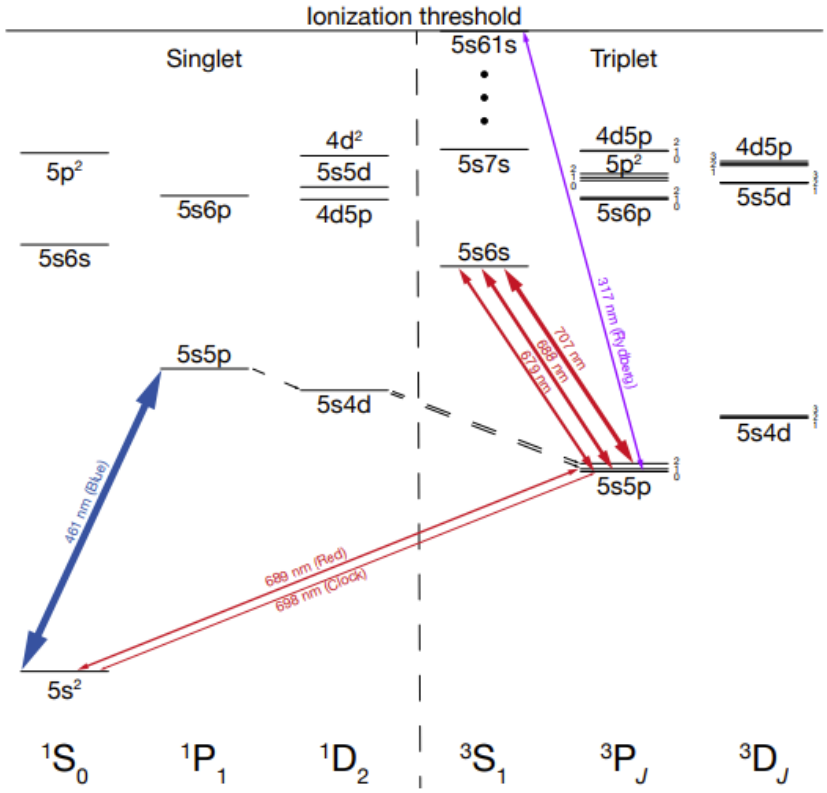

Figure 2.1: Lowest-lying energy levels of Strontium. Picture taken from [15].

As it happens in other alkaline-earth atoms, Strontium features the presence of intercombination transitions that connect triplet and singlet states, which in first approximations would be prohibited by the selection rules, and therefore have narrow and ultra-narrow linewidths, and the presence of metastable states characterized by long lifetime. These characteristics are relevant both for cooling and excitation schemes.

The first transition of interest for the experiment is the blue ${}^1S_0 \rightarrow {}^1P_1$ at a wavelength of 461 nm, this transition is employed both for slowing, for the first stage of MOT and for the imaging scheme.

The ${}^1S_0 \rightarrow {}^3P_1$ red intercombination line at 689 nm is used for the second stage of MOT since the linewidth of this transition is $\Gamma = 2\pi 7.6\,\mathrm{kHz}$, allowing for a cooling

of the atoms down to very low Doppler temperatures on the order of hundreds of nK, much lower than those achievable for alkali atoms with the Doppler cooling only [15]. Furthermore, the presence of the clock state $^3P_0$, connected with the ground state $^1S_0$ by an ultranarrow transition, can be used in atomic clock experiments to reach extremely high precision measurements [16, 17], and can be employed in the realization of optical qubits.

The clock transition $5s^2\,^1S_0 \leftrightarrow 5s5p\,^3P_0$ is strictly dipole forbidden by both the $J = 0 \rightarrow J' = 1$ and $\Delta S = 0$ electric dipole selection rules. In order to drive the clock transition, it is necessary to break the rotational symmetry and admix the unperturbed clock state with a state that has $J = 1$ ($5s5p\,^3P_1$ with $m_J = 0$) with, either naturally, as it happens as a result of the hyperfine interaction in the case of the fermionic isotope, or, in the case of the bosonic isotopes a magnetic field [18]. In the latter case, this admixture (with $5s5p\,^3P_1$, $m_J = 0$) gives the perturbed clock state a finite decay rate [15]:

$$\Gamma_{clock}(B) = \Gamma_{^3P_1} \frac{\mu_C^2 B^2}{\hbar^2 \Delta_{01}^2} \tag{2.1}$$

which is proportional to B^2, where Δ_{01} is the splitting between $^3P_0$ and $^3P_1$, $\Gamma_{^3P_1}$ is the decay rate of the $5s5p\,^3P_1$ state and $\mu_C \equiv \sqrt{\frac{2}{3}}(g_L - g_S)\mu_B$ is a constant, with $\mu_B = 9.27 \times 10^{-21} \frac{\text{erg}}{G}$, $g_L \simeq 1$ and $g_s \simeq 2$. This admixture allows for a finite dipole coupling with the ground state $5s^2\,^1S_0$, with a Rabi frequency that scales linearly with B:

$$\Omega_{clock} = \frac{\mu_C B}{\hbar \Delta_{01}} \sqrt{\frac{3\Gamma_{^3P_1}\lambda^3 I}{4\pi^2 \hbar c}} (\hat{\epsilon} \cdot \hat{B}) \tag{2.2}$$

where $\lambda = 698\,nm$ is the wavelength of the transition, I is the intensity of the optical beam and $\hat{\epsilon} \cdot \hat{B}$ is the projection of the polarization of the excitation beam in the direction of the magnetic field. A robust excitation to the clock state is crucial for future experiments that can be implemented with this platform. The ability to excite the clock state on sub-ms timescales allows it to be used within experiments with tweezer atoms that have an experimental cycle duration of the order of $\sim 100\,\text{ms}$. In order to have pulses with a duration of 1 ms, we must achieve at least a Rabi frequency of 500 Hz. In this way the clock state can be used as a ground state to realize the excitation towards the Rydberg state and study magnetic models [16]. Or it can be used as one of the two states forming a qbit, together with the ground

state, to realize fast quantum gates [19].

2.2 Excitation towards the Rydberg state

In the platform on which this thesis is focused the Strontium atoms are trapped in an array of microscopic dipole traps separated by a few micrometers. Neutral ground-state atoms do not interact via Coulomb interaction, since they have no net charge. Dipole-dipole interactions are also negligible because of the zero electron spin in the ground state of Strontium atoms. To make them interact at a distance larger than a micrometer, the atoms are excited to Rydberg states, i.e. states with high principal quantum number n and a macroscopically large wave function [20, 21]. In table 2.2 some of the properties of the Rydberg states scaling with the principal quantum number are reported.

Property	n-scaling
Binding energy E_n	n^{-2}
Level spacing $E_{n+1} - E_n$	n^{-3}
Size of the wavefunction $\langle r \rangle$	n^2
Lifetime τ	n^3
Van der Waals coefficient C_6	n^{11}

Table 2.2: Scaling of Rydberg states properties on the principal quantum number.

When the atoms are in Rydberg states they exhibit a large electric dipole moment, which leads to strong long-range interactions. Two Rydberg atoms, separated by a distance R, can interact via dipole-dipole or Van der Waals interaction depending on how the pair is prepared.

If the two atoms are prepared in two different Rydberg levels, such as $|n, S\rangle$ and $|n, P\rangle$ (with same principal quantum number and different projection of the angular momentum, in order to have the closest possible energy between the levels) they interact via the electric dipole-dipole Hamiltonian:

$$\hat{V}_{dd} \sim \frac{\hat{d}_1 \hat{d}_2}{4\pi\varepsilon_0 R^3} \tag{2.3}$$

where d_i is the electric dipole moment of the atom i and ε_0 is the permittivity of vacuum.

When two atoms are excited to the same Rydberg level, $|n, S\rangle$ as an example, the Hamiltonian 2.3 has no effect at first order in perturbation theory because of parity. The effect of the interaction is of second order, where the pair state $|nS, nS\rangle$ is coupled to other pair states of opposite parity via the interaction Hamiltonian $\hat{V}_{dd}$. The main contribution to the second-order correction comes from the closest energy level (the one with the same principal quantum number but different angular momentum). The resulting energy shift is proportional to $\frac{V^2}{\Delta}$, where Δ is the detuning from the target level and $V \propto \frac{d_1 d_2}{R^3}$ is the matrix element. This gives rise to a van der Waals shift of the pair state:

$$\Delta E_{vdW} \propto \frac{V^2}{\Delta} \propto \frac{C_6}{R^6} \tag{2.4}$$

where C_6 is the van der Waals coefficient, which is on the order of $\frac{d^4}{\Delta}$. Since the electric dipoles matrix elements scales as $d \sim n^2$ and the separation between next levels as $\Delta \sim n^3$, C_6 scales as n^{11}. The van der Waals interaction between two Rydberg atoms can reach tens of megahertz for $n \simeq 50$ atomic separation of several micrometers [8].

2.3 Rydberg blockade mechanism

The interaction between atoms excited towards Rydberg states can be very strong. This interaction leads to a mechanism called "Rydberg blockade", in which the simultaneous excitation of multiple atoms is suppressed. This mechanism can be employed in the realization of entangled states.

To better understand how this mechanism works, let's consider a resonant laser field coherently coupling the ground state $|g\rangle$ and a given Rydberg state $|r\rangle$, with a Rabi frequency Ω as shown in figure 2.2 on the left. If we consider two atoms separated by a distance R (figure 2.2 right), when the atoms are excited towards the Rydberg state, due to the strong van der Waals interaction, the doubly excited state $|rr\rangle$ energy is shifted by the quantity $\frac{C_6}{R^6}$, with C_6 being the interaction coefficient. If the distance between the atoms R is less than the blockade radius R_b (defined below) the coupling to the doubly excited state $|rr\rangle$ is now non-resonant and thus suppressed. Starting from the ground state $|gg\rangle$ the system evolves to the collective

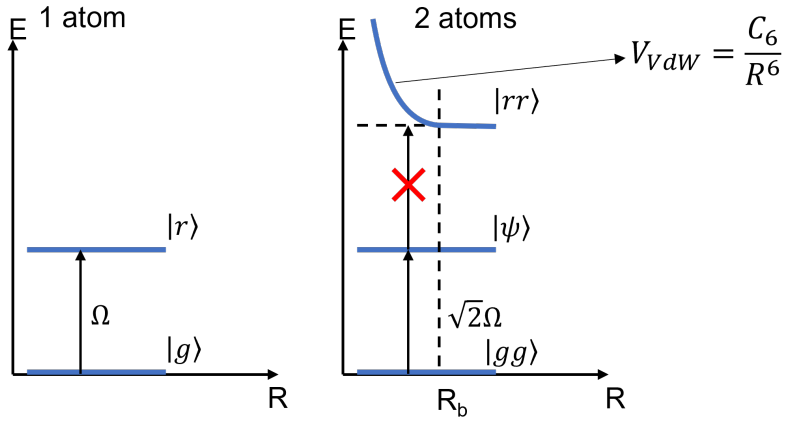

Figure 2.2: Ground $|g\rangle$ and Rydberg $|r\rangle$ state of a single atom coupled by a resonant laser with Rabi frequency Ω (left). Energy shift with consequent suppression of the double Rydberg excitation due to the strong van der Waals interaction between two close enough atoms (right).

state:

$$|\psi\rangle = \frac{1}{\sqrt{2}}\left(|gr\rangle + |rg\rangle\right)$$

with a coupling $\sqrt{2}\Omega$. This leads to a collective Rabi oscillation at frequency $\sqrt{2}\Omega$ between $|gg\rangle$ and the entangled state $|\psi\rangle$. The condition that defines the blockade radius is when the van der Waals energy equals the Rabi coupling $\hbar\Omega = \frac{C_6}{R^6}$, letting to:

$$R_b = \left(\frac{C_6}{\hbar\Omega}\right)^{\frac{1}{6}}$$

What has just been described for two atoms can be easily extended to an ensemble of N atoms included within a blockade volume. In this case only one of the atoms can be excited to the Rydberg state, and this leads to collective Rabi oscillations between the collective ground state $|g...g\rangle$ and the entangled state $\frac{1}{\sqrt{N}}\left(|rg...g\rangle + |gr...g\rangle + \cdots |gg...r\rangle\right)$ with an enhanced frequency $\sqrt{N}\Omega$. In the entangled state the Rydberg excitation is shared among all the atoms. If the system size is larger than the blockade volume, as shown in figure 2.3, it is possible to excite more than one atom to the Rydberg state, but the positions of the excited atoms will be strongly correlated with each other, due to the blockade constraint, and this gives rise to complex many-body dynamics.

Entangled states are key resources in many experimental applications, such as

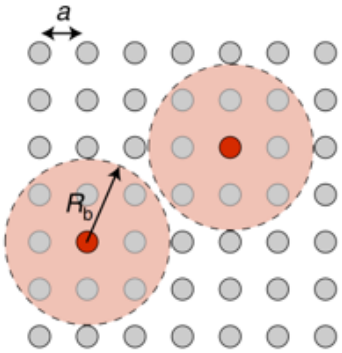

Figure 2.3: In a large ensemble of atoms, an atom excited to the Rydberg state prevents the excitation of all the other atoms within the blockade radius. Image taken from [8].

quantum metrology, where these states are exploited to enhance the precision of experimental measurements [22], or the realization of multi-qubit entangling gates for high-fidelity quantum information processing [19].

2.4 Rydberg atoms in optical tweezers

In this platform the atoms are trapped in an array of optical tweezers, which are optical dipole traps realized by tightly focusing far-off resonant beams of light trough a high numerical aperture objective lens [23]. These traps have a small volume, typically $\leq 1\,\mu\text{m}^3$, and a maximum of one atom can be trapped in each tweezers. If two atoms enter the same tweezer a mechanism of light-assisted collision, called "collisional blockade", causes the ejection of both of them from the trap [24, 25].

Arrays of optical tweezers can be realized using spatial light modulators (SLMs) and acusto-optic deflectors (AODs). SLMs are devices that exploit a liquid crystal as a phase mask for the light beam, working with holographic techniques to imprint a phase pattern on the input beam that hits the SLM's screen, in order to obtain a certain spatial pattern in the conjugate plane, allowing for the realization of any static geometry of the array. For the realization of defect-free array of atoms, since the collisional blockade provides a probability of $\sim 50\%$ for the traps occupation, a rearrangement is required. It is realized using two crossed AODs [26], which are devices driven by an RF signal that can diffract a laser beam with an angle dependent on the frequency of the RF signal. Using a time-dependent RF signal it

is possible to move the diffracted laser beam and use it for the rearrangement of the atoms trapped in the optical tweezer arrays realized with the SLM. This happens by steering the atom one by one from their initial trap to the final target positions. Some examples of arbitrary defect-free arrays made this way are illustrated in figure 2.4.

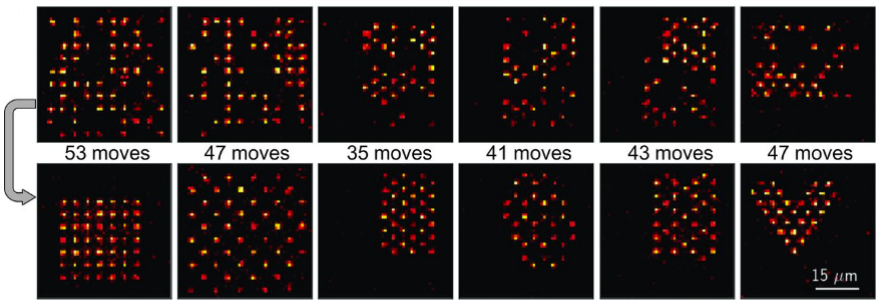

Figure 2.4: Arbitrary 2D arrays obtained from the initial random configurations with a rearrangement procedure. Image taken from [26]

This platform guarantees a high degree of control both on the geometry of the system and on the interaction and internal degree of freedom of the atoms. The two types of interaction that can occur between Rydberg atoms, van der Waals and dipolar, are naturally suitable for the simulation of quantum spin Hamiltonians.

In the case of atoms excited to the same Rydberg level, the dipole interaction leads to the van der Waals interaction. If we map the ground $|g\rangle$ and Rydberg $|r\rangle$ state of each atom onto a spin $\frac{1}{2}$ model:

$$|g\rangle = |\downarrow\rangle$$
$$|r\rangle = |\uparrow\rangle$$

the Hamiltonian of an ensemble of atoms driven by a coherent laser, with Rabi frequency Ω and detuning δ, is [27]:

$$H = \frac{\hbar\Omega}{2}\sum_i \sigma_x^i - \hbar\delta\sum_i n_i + \sum_{i<j} V_{ij} n_i n_j \tag{2.5}$$

with $V_{ij} = \frac{C_6}{R_{ij}^6}$ being the van der Waals interaction, which depends on the separation $R_{i,j}$ between atoms in sitse i and j, $\hbar$ is the reduced Planck constant, σ_x^i is the Pauli matrix and $n_i = |r_i\rangle\langle r_i|$ is the operator that counts the number of excitations in

the site i. Since the relation $n_i = \frac{(\sigma_z^i+1)}{2}$ holds, the Hamiltonian 2.5 has the form of the quantum Ising model, where the frequency and detuning terms are respectively the transverse and longitudinal fields, and the van der Waals interaction is the Ising coupling.

When the atoms are prepared in two different Rydberg levels, $|nS\rangle$ and $|nP\rangle$ as an example, typically separated by a transition frequency of a few GHz, the interaction is dipolar. In this case the spin basis can be mapped in the two different Rydberg states, having:

$$|nS\rangle = |\downarrow\rangle$$
$$|nP\rangle = |\uparrow\rangle$$

Microwave radiation can be used to manipulate the spin and acting as an effective magnetic field. Thus the Hamiltonian of an ensemble of atoms subject to the dipole-dipole interaction can be identified with the following XY Hamiltonian:

$$H = \frac{\hbar\Omega_{\mu w}}{2}\sum_i \sigma_x^i - \frac{\hbar\delta_{\mu w}}{2}\sum_i \sigma_z^i + \sum_{i\neq j}\frac{C_3}{R_{ij}^3}(\sigma_+^i\sigma_-^j + \sigma_-^i\sigma_+^j) \tag{2.6}$$

where $\sigma_+ = \frac{1}{2}(\sigma_x + i\sigma_y)$ and $\sigma_- = \frac{1}{2}(\sigma_x - i\sigma_y)$. Here the transverse and longitudinal fields are given by the Rabi frequency $\Omega_{\mu w}$ and the detuning $\delta_{\mu w}$ of the microwave field, especially, while the interaction term is given by the dipole-dipole interaction.

The greatest advantage offered by Rydberg atoms in optical tweezers is the high degree of access to the experimental parameters as well as the control over individual quantum objects.

An example of Ising model simulation is the one realized by Bernier et al [9], where a programmable Ising-type quantum spin model with tunable interaction was achieved in a linear array of atoms as a function of the parameters of the Ising Hamiltonian 2.5, which are fully controllable. In figure 2.5 we show a result of that experiment, where it is possible to observe a phase transition into spatially ordered states tuning the ratio $\frac{\Delta}{\Omega}$ between the detuning and the Rabi frequency, which represent the external magnetic field components. Furthermore, changing the ratio $\frac{R_b}{a}$ between the blockade radius and the trap spacing different ordered phases are encountered. The phase diagram is obtained as a function of the Hamiltonian parameters by the direct measurement of correlation functions with single-site resolution. For negative values of the detuning Δ the configuration that minimizes the energy for the Hamiltonian 2.5 is the one that minimizes the number of Rydberg

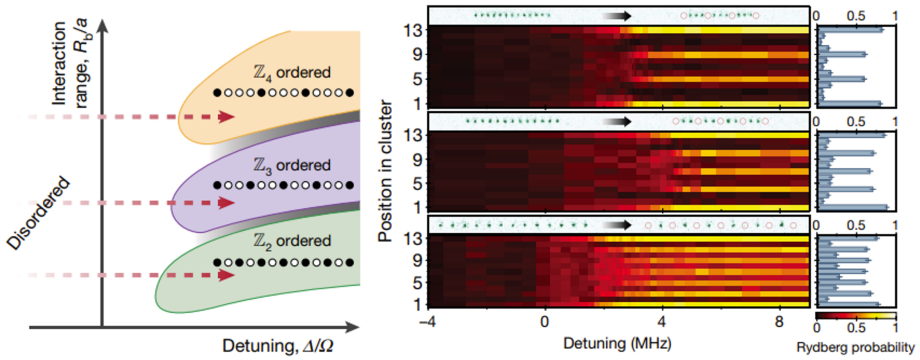

Figure 2.5: Schematic phase diagram as a function of the Hamiltonian parameters (left). Single-shot fluorescence image before and after the Rydberg excitation pulse (middle). Bar plot displaying the final position-dependent Rydberg probability(right). Image taken from [9].

atoms n_i, while for large detuning it is convenient to have as many excited atoms as possible, within the constraint of the Rydberg blockade. The three plots in figure 2.5 are realized for $R_b \sim a\,, 2a\,, 3a$, where a is the distance between traps, in such a way that one, two and three neighbors of the Rydberg atom are blockaded.

Furthermore, the possibility that this platform offers to directly measure the properties of atoms in real time, makes it also suitable for the study of coherent dynamics of many-body system far from equilibrium. In a different experiment reported in [9] the system is first adiabatically prepared in an ordered state, then the detuning is suddenly quenched to the single-atom resonance $\Delta = 0$ and interesting dynamics show up: in figure 2.6 it is possible to observe the oscillation of many-body states between the initial antiferromagnetic state and the complementary one (atoms in the ground state ended up in the Rydberg state and vice versa).

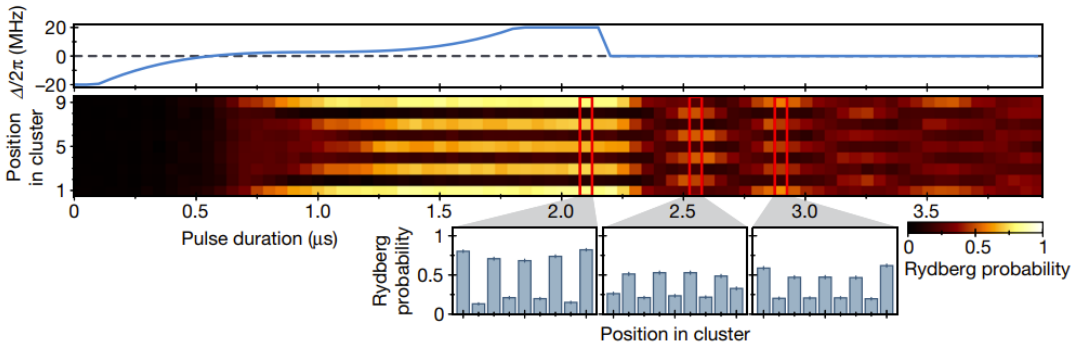

Figure 2.6: Out-of-equilibrium dynamics in a linear array of atoms. Image taken from [9].

Chapter 3

Cooling and trapping

This chapter provides an overview of the main aspects of laser cooling and trapping that are employed in the realization of the experiment. Laser cooling techniques, which exploit the interaction between the atoms and the radiation emitted by a laser source, allow for extremely low temperatures to be reached, down to the order of μK [28]. The idea is to decrease the kinetic energy of the atoms by transferring part of their energy to the electromagnetic field. With related techniques the cooled atoms can also be confined in "traps", delimited not by material walls but by electromagnetic fields.

3.1 Deceleration of an atomic beam

The typical source for experiments with cold atoms is an atomic beam, generated by heating up a solid sample in an oven. The atoms exit the oven through a hole and generate a flow with a certain direction and a non-thermal velocity distribution. To slow down the atoms we can exploit the radiation pressure generated by a laser beam. The simplest configuration that we can imagine is the one in which a laser beam propagates in the opposite direction of the atomic beam.

The radiation pressure force generated by a single laser beam, with wave vector $\mathbf{k}$ and intensity I, can be written as:

$$\mathbf{F} = \hbar\mathbf{k}\,\frac{\gamma}{2}\,\frac{S}{S+1}\,\frac{1}{1+\left(\frac{2\delta}{\gamma_S}\right)^2} \tag{3.1}$$

with S being the saturation parameter, defined as $S = \frac{I}{I_{sat}} = \frac{2\Omega^2}{\gamma^2}$, that quantifies the intensity in terms of the saturation intensity I_{sat}, which is proportional to γ, the linewidth of the atomic transition. Ω is the Rabi frequency and $\gamma_S = \gamma\sqrt{1+S}$ is the saturated linewidth. The detuning δ is defined as the difference between the laser frequency ω and the frequency of the atomic transition ω_0. Because of the Doppler effect the detuning becomes:

$$\delta = \omega + kv_0 - \omega_0 \tag{3.2}$$

with v_0 being the initial velocity of an atom in the atomic beam. The force in equation 3.1 is maximum when $\delta = 0$, then:

$$\omega - \omega_0 = -kv_0 \tag{3.3}$$

In order to compensate the positive Doppler shift we must impose a negative detuning in the laser beam. The radiation pressure force reduces the velocity of the atom v_0, in this way, however, we lose the condition $\delta = 0$ for which we have the maximum of the force. Rewriting the condition for a generic, non constant, velocity v of the atoms we obtain:

$$\delta = \omega + kv - \omega_0 = 0 \tag{3.4}$$

a possible solution to keep this condition while the atomic beam decelerates is to vary the frequency of resonance $\omega_0(x)$ in space.

3.2 Zeeman slower

A widely used technique to make the frequency ω_0 change uses magnets to generate a non-homogeneous magnetic field and the Zeeman effect to keep the laser consistently resonant with the atoms. This is called "Zeeman slower" and was demonstrated for the first time with Sodium [29].

For an atom interacting with a magnetic field B the Hamiltonian describing the interaction has the form:

$$H_Z = -\boldsymbol{\mu} \cdot \mathbf{B}$$

with $\boldsymbol{\mu}$ being the magnetic dipole moment given by:

$$\boldsymbol{\mu} = -\frac{\mu_B}{\hbar}\mathbf{l} - g_s\frac{\mu_B}{\hbar}\mathbf{s} + g_I\frac{\mu_N}{\hbar}\mathbf{I}$$

where $\mathbf{l}$ and $\mathbf{s}$ are the orbital angular momentum and the spin angular momentum of the electron and $\mathbf{I}$ is the spin angular momentum of the nucleus. μ_B and μ_N are the Bohr magneton and the nuclear magneton, respectively. The interaction with the magnetic field breaks the degeneracy and sets a privileged direction in the space. The separation of energy levels due to an external magnetic field is called the Zeeman effect.

Due to the Zeeman effect the resonant frequency of an atom is varied by a quantity:

$$\frac{\Delta\mu B}{\hbar} = \frac{(\mu_g - \mu_e)B}{\hbar}$$

where μ_g and μ_e are the magnetic dipole moments of the ground state and of the excited state, respectively. Using a non-homogeneous magnetic field $B(x)$ the shift will depend on the position. Now the detuning can be written as:

$$\delta(v) = \omega + kv - \left(\omega_0 + \frac{\Delta\mu}{\hbar}B(x)\right) \qquad \forall x, v \tag{3.5}$$

and a suitable magnetic field can be used to keep the condition $\delta = 0$ always satisfied in space, and the radiation pressure becomes a constant force:

$$\mathbf{F} = \hbar\,\mathbf{k}\,\frac{\gamma}{2}\,\frac{S}{S+1} \tag{3.6}$$

which allows for an effective slowing down of the atomic beam.

The radiation force has a linear dependence on the linewidth γ of the atomic transition. In the case of the Strontium, a blue laser beam at 461 nm is used to realize the Zeeman slower. The excited transition is the ${}^1S_0 \rightarrow {}^1P_0$, which has a width of 32 MHz, higher than the linewidth of the intercombination transition. This allows the atomic beam to be slowed down more effectively over shorter lengths.

3.3 Doppler cooling

Another way to slow down atoms is the Doppler cooling technique, introduced in 1975 by Hänsch e Schawlow [30]. The framework to understand Doppler cooling involves an atom traveling at velocity v in a light field originated by two counter-propagating laser beams with intensity I, wavevectors $\pm\mathbf{k}$ and frequency ω (figure 3.1).

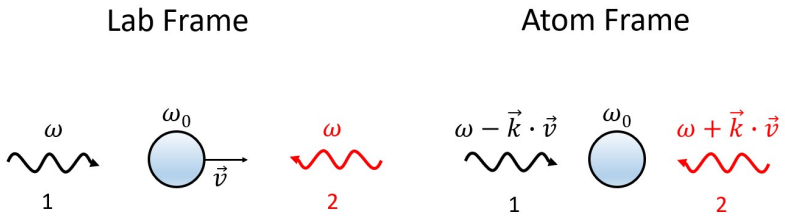

Figure 3.1: Scheme for the Doppler cooling of an atom with velocity v with two counter-propagating beams.

Assuming to be in the red detuning regime $\delta = \omega - \omega_0 < 0$, because of the Doppler effect the frequency of the two beams are shifted differently:

$$\begin{aligned} \delta_1 &= \omega - kv - \omega_0 \\ \delta_2 &= \omega + kv - \omega_0 \end{aligned} \tag{3.7}$$

This Doppler shift creates an imbalance in the absorption rate of the photons between the two beams and hence the imbalance of the radiation pressures, which allows the atom to be slowed down.
The velocity-dependent radiation pressure force is:

$$\begin{aligned} \mathbf{F} = \mathbf{F}_1 + \mathbf{F}_2 &= \hbar\mathbf{k}\frac{\gamma}{2}\frac{S}{S+1}\frac{1}{1+\left(\frac{2\delta_1}{\gamma_s}\right)^2} - \hbar\mathbf{k}\frac{\gamma}{2}\frac{S}{S+1}\frac{1}{1+\left(\frac{2\delta_2}{\gamma_s}\right)^2} = \\ &= \hbar\mathbf{k}\frac{\gamma}{2}\frac{S}{S+1}\left[\frac{1}{1+\frac{4(\omega-kv-\omega_0)^2}{\gamma_s^2}} - \frac{1}{1+\frac{4(\omega+kv-\omega_0)^2}{\gamma_s^2}}\right] \end{aligned} \tag{3.8}$$

An example of this force is plotted in figure 3.2.

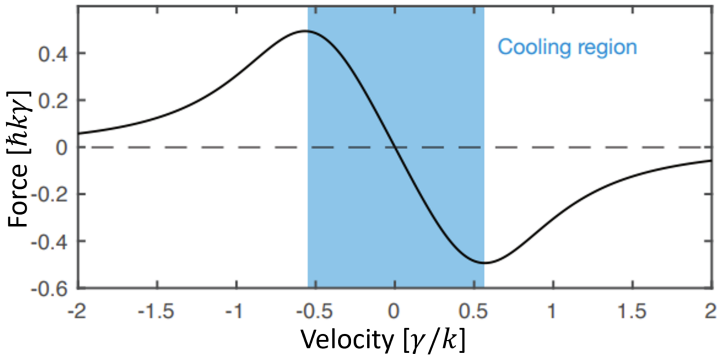

Figure 3.2: Dependence of the light force on the velocity of the atom for two counter-propagating red-detuned laser beams. The blue zone represents the efficient cooling region. Figure taken from [31].

The maxima of the force correspond to the capture rate:

$$v_c = \frac{|\delta|}{k} \tag{3.9}$$

obtained by imposing $\delta - kv = 0$. The capture rate defines the rate below which the atom can be slowed down and cooled. If the atoms are traveling with a speed $|v| > v_c$ they will not be slowed down efficiently. The equation 3.8 is valid if we assume that we are in a low saturation regime $S \ll 1$, which allows us to consider that the two beams induce independent effects on the atoms.

The saturation is the process that occurs when a very intense laser beam induces a stationary change in the population of a two-level system. Under the $S \ll 1$ condition we can assume the entire population in the ground state, that corresponds to $\gamma \gg \Omega$, a condition that involves an emission rate much higher than the absorption rate, i.e. as soon as it is excited, the atom immediately decays in the ground state. When this happens we can consider the effects of the two beams as independent of each other, since the excitation by one of the two beams is so short that it does not affect the effects of the other. If, on the other hand, we had saturation with $S \gtrsim 1$, the absorption and emission rates would be comparable and we would have a part of the population blocked in the excited state and no longer available to be excited

by the beams. Therefore, assuming the condition of $S \ll 1$ we can also consider:

$$\frac{S}{S+1} \simeq S$$
$$\gamma_s \simeq \gamma$$

and the force can be written as:

$$\mathbf{F} \simeq \alpha \mathbf{v} + o(v^3) \tag{3.10}$$

finding the shape of a friction force with a Doppler coefficient:

$$\alpha = -8\hbar k^2 S \frac{\delta/\gamma}{\left(1+\frac{4\delta^2}{\gamma^2}\right)^2} > 0 \tag{3.11}$$

This damping force is effective until quantum fluctuations of the force, due to the stochastic nature of spontaneous emission and to the laser intensity shot noise, set in. When these effects are considered, it can be shown [32] that the velocity distribution of the atoms approaches a thermal Maxwell-Boltzmann distribution characterized by a Doppler temperature, whose minimum value:

$$T_{Doppler} \approx \frac{\hbar\gamma}{2k_B} \tag{3.12}$$

can be reached for a detuning $\delta = \frac{\gamma}{2}$.

The minimum value for the Doppler temperature in equation 3.12 has a linear dependence on the linewidth γ of the atomic transition. For this reason in useful to exploit ultranarrow intercombination transition in order to obtain lower temperatures. On the other hand the capture velocity (equation 3.9) is also reduced as γ decrease allowing the trapping of only a reduced class of atoms with lower velocity. The experimental strategy is then to have two sequential laser cooling stages. A first stage is realized exploiting the ${}^1S_0 \rightarrow {}^1P_1$ transition of strontium, which has a linewidth of 32 MHz, and enables robust pre-cooling of atoms in a large velocity range with $T_{Doppler} \approx 800\,\mu$K. A second stage is then realized using the a ${}^1S_0 \rightarrow {}^3P_1$ transition, which has a linewidth of 7.6 kHz and temperatures of about $T_{Doppler} \approx 200\,$nK can be reached.

3.4 Magneto-Optical Trap

To trap the atoms at this cold temperatures, not only within a specific velocity range but also confining them in space, it is necessary to realize an atomic trap, with a physical mechanism that allows the breaking of the spatial symmetry with a restoring force attracting the atoms towards a trap center.

A magneto-optical trap is realized exploiting six red-detuned counter-propagating laser beams in the three directions and a three-dimensional magnetic field gradient to lift the degeneracy between magnetic sublevels to scatter spatial dependent photons from certain beams. For the sake of simplicity we can consider a one-dimensional case, which can then be easily extended into three dimensions, a scheme is reported in figure 3.3.

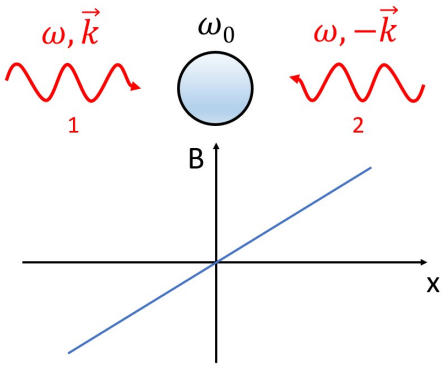

Figure 3.3: Experimental configuration of a magneto-optical trap in the one-dimensional case with linear magnetic field.

In order to understand the operation of a magneto-optical trap we consider a simplified case of a transition from a ground state $|g\rangle$ with total angular momentum $F_g = 0$ to an excited state $|e\rangle$ with $F_e = 1$, therefore a closed transition with $\Delta F = 1$. Let us consider a magnetic field with a linear dependence on the position in space along x:

$$\mathbf{B} = bx\hat{x} \tag{3.13}$$

This field induces a Zeeman shift to the atom's energy levels, which can be used to generate a restoring force to trap the atom. The magnetic structure of the ground state is not modified, while in the excited state it is modified, since there are three different $m_{F_e} = 0, \pm 1$ states. As the magnetic field depends on position, the energetic

shift of the levels of the excited state will depend on position too (figure 3.4):

$$\Delta E(x) = g_{F_e} \mu_B b x m_{F_e} \tag{3.14}$$

For the MOT to work, the beams must have circular polarization with opposite sign, σ^- for the beam coming from the right and σ^+ for the one coming from the left in figure 3.3.

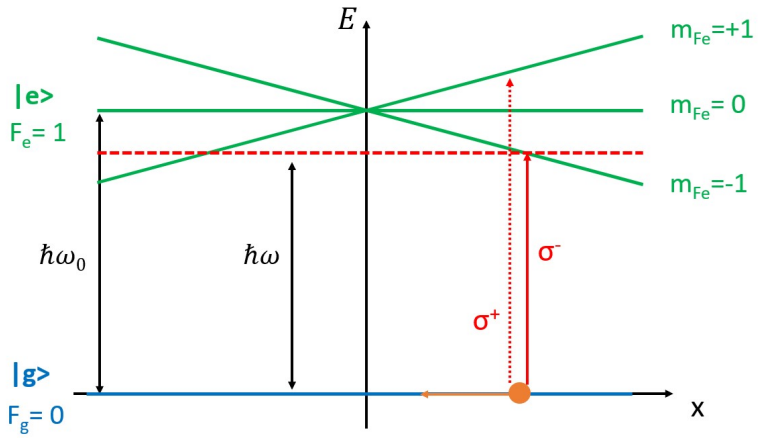

Figure 3.4: Structure of the energy levels and transitions involved in the realization of a MOT. The ground $|g\rangle$ state is represented with the blue line, the excited state $|e\rangle$ with its magnetic structure is represented with green lines. The red dashed line represents the energy of the incident photon. The dashed and solid red arrows are the two transitions respectively for the σ^+ and σ^- polarized beams. The orange point represents the position of the atom and the orange arrow is the restoring force directed towards the trap center.

Referring to the figure 3.4, let's consider an atom in a certain position $x > 0$. The selection rules impose that the σ^+ polarized beam induces a transition towards the $m_{F_e} = 1$ state, while the σ^- polarized beam induces a transition towards the $m_{F_e} = -1$ state. Since the laser beams are red detuned, two different photons, coming from two different laser beams, have different detuning in presence of the magnetic field since they are coupled to states with different energies because of the opposite sign of the Zeeman energy shift. In this case the transition induced by the σ^- polarized beam is the most probable (if we had considered an atom in position $x < 0$ the treatment would have been analogous but the most probable transition would have been the one induced by the σ^+ polarized beam). So the atom experiences a force of radiation pressure, directed from right to left for $x > 0$

(opposite direction if $x < 0$), which pushes the atom towards the position $x = 0$ corresponding to the trap center.

Similarly to what we did for the Doppler cooling, in the case of a one-dimensional trap, the force can be written as:

$$\mathbf{F} = \frac{\hbar \mathbf{k} \gamma S}{2} \left[\frac{1}{1 + \left(\frac{2(\omega - (\omega_0 + g_{F_e} \mu_B b x) - kv)}{\gamma} \right)^2} - \frac{1}{1 + \left(\frac{2(\omega - (\omega_0 - g_{F_e} \mu_B b x) + kv)}{\gamma} \right)^2} \right] \tag{3.15}$$

This is the one-dimensional case with a linear magnetic field, which can be easily extended in the three-dimensional case. The force depends both on the velocity and on the position of the atoms, allowing both for the cooling and for the trapping of the atoms.
By linearizing the velocity and spatial dependency, the force can be written as:

$$\mathbf{F}(x, v) \simeq (-M\Omega^2 x - \alpha v)\hat{x} \tag{3.16}$$

The force has two terms, one proportional to position and one to velocity. The velocity-proportional term is a friction force with the same α coefficient as the Doppler cooling (with $\delta < 0$):

$$\alpha = -8\hbar k^2 S \frac{\delta}{\gamma \left(1 + 4\frac{\delta^2}{\gamma^2}\right)^2} > 0 \tag{3.17}$$

The term proportional to the position is instead the restoring force, it has the same shape as a harmonic oscillator, and is directed towards the trap center. A Trap Frequency can be defined as:

$$\Omega^2 = \frac{g_{F_e} \mu_B b}{\hbar k M} \alpha \tag{3.18}$$

The system can therefore be considered as a damped harmonic oscillator. So, for a given gradient of magnetic field, the capture volume of the trap and the velocity of the trapped atoms will both depend on the linewidth γ of the transition.

Again, the considerations made in the previous section apply, the trapping is realized with a double 3D-MOT stage. The first one on the broad blue transition ${}^1S_0 \rightarrow {}^1P_1$ and the second one on the red narrow intercombination transition ${}^1S_0 \rightarrow {}^3P_1$ to maximize the number of trapped atoms and minimize their temperature.

Chapter 4

Overview on the experimental setup

In this chapter I will provide a description of the experimental setup. A drawing of the vacuum apparatus employed for the realization of the experiment is shown in figure 4.1. It is designed to be as simple and compact as possible while maintaining properties such as high vacuum lifetimes and optical access. It is composed of three main components: the atomic source, the pumping chamber and the glass cell where the "real" experiment is performed.

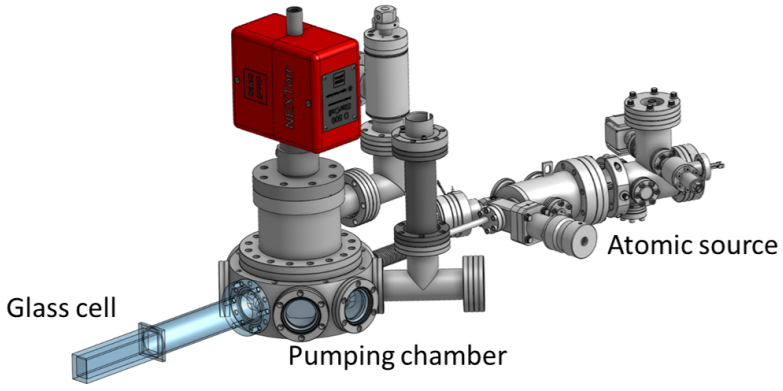

Figure 4.1: Drawing of the experimental apparatus with the main components.

4.1 The atomic source

The atomic source is a commercial solution from AOSense (also illustrated in figure 4.2).

At room temperature Strontium is in the solid state and its vapor, from which the atomic beam is extracted, has a negligible pressure. In order to increase the vapor pressure, and consequently the atomic beam flow, the solid sample must be heated up to a temperature closer to the melting temperature $T_{mel} \simeq 1050$ K (indeed, the vapor pressure of any substance in the solid state increases almost exponentially with temperature). There is an nozzle oven in the source that heats up the atomic strontium and pre-collimates the extracted atomic beam with capillaries.

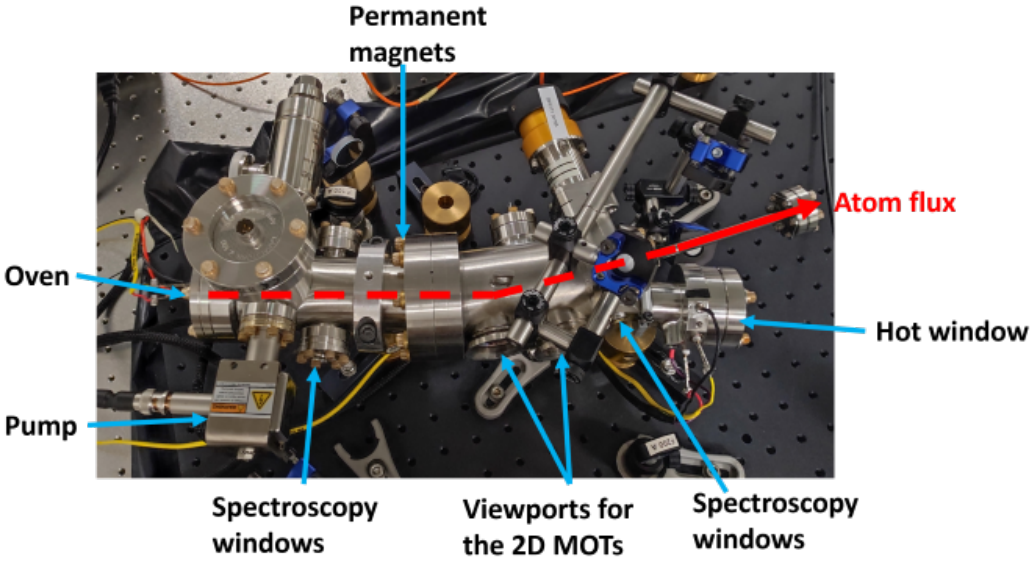

Figure 4.2: Picture of the atomic source.

In addition to the oven, the commercial atomic source includes:

- A pump, to maintain the high vacuum condition inside the source.
- A set of permanent magnets for the generation of magnetic fields, employed in the realization of two 2D MOTs and of the Zeeman slower.
- A hot window used to send the blue beam for the Zeeman slower in the source. It is heated up to prevent the formation of a film of Strontium on it.
- Two viewports and internal mirrors for the realization of two 2D MOTs.
- Two sets of windows for spectroscopy, the first one with bigger windows near the oven and the other one with smaller windows near the hot window.

The first set of spectroscopy windows are used to observe the uncooled atomic beam from the oven, providing a way to test the performance of the oven itself. Some of these measurements are illustrated in the section 6.2.2. Following the spectroscopy windows, the atomic beam passes through the set of permanent magnets, which, combined with a blue laser beam, reduce the velocity of a fraction of the atoms to speeds that can be easily captured by the MOT, as explained in section 3.2. After the Zeeman slower the two viewports are employed for the generation of two 2D MOTs that, not only cool down the atoms in the transverse direction, but are also used to deviate the atomic beam from its initial direction of propagation. This is useful in order to separate colder strontium atoms from the hotter ones that aren't deviated and end up in the hot window. This deviation also prevents hot atoms or hot background gases produced from the oven to reach the pumping chamber and the glass cell. Since there is not direct line-of-sight from the glass cell to the oven the blackbody radiation from the oven is also suppressed. Furthermore the 2D MOTs can act as a convenient and fast optical switch for turning the atomic flux to the glass cell on and off, requiring no mechanical shutter. The second set of spectroscopy windows, near the hot window, is employed for the frequency lock of the 461 nm laser, as shown in section 6.2.4. The pump integrated in the atomic source is required for the maintenance of the vacuum condition. Varying the temperature of the oven from 420°C to 500°C the pressure in the source changes from 9.1×10^{-9} Torr to 7.7×10^{-8} Torr.

The source is connected to the pumping chamber through a differential pumping stage, to provide a high pressure gradient in order to minimize the pressure in the apparatus. This is fundamental for the achievement of long lifetimes of the atomic ensembles, since the main source of losses are collisions with the background gas. The main contribution to the pressure increase in the glass cell is due to outgasing hydrogen from the components of the apparatus. Altough a baking of all these components will be realized, the outgasing will never be completely absent, especially because the glass cell cannot be baked at too high temperatures. To achieve a pressure on the order of 5×10^{-11} Torr in the glass cell we estimated that a pumping speed of 500 L/s in the pumping chamber is required. We chose a NEXTorr D500-StarCell pump for the chamber.

4.2 Experimental sequence

The core of the entire experiment is the glass cell. Here the Strontium atoms are trapped first in a MOT realized on the broad blue transition, ${}^1S_0 \rightarrow {}^1P_1$ with a linewidth $\Gamma = 2\pi\, 32\,\mathrm{MHz}$, then they are trapped in a much colder and denser MOT on the narrow red transition, ${}^1S_0 \rightarrow {}^3P_1$ with a linewidth $\Gamma = 2\pi\, 7.6\,\mathrm{kHz}$, small enough to cool the atoms down to a few hundreds nK [15]. Two different MOTs with different linewidth and thus acting on different velocity ranges are realized in order to maximize the number of trapped atoms (with the blue MOT) and minimize their velocity (with the red MOT).

The array of optical tweezers is overlapped to the MOTs and the atoms are loaded in the tweezers dipole traps. Here pairwise losses take place (as explained in section 2.4) and, thanks to this collisional blockade mechanism, no more than one atom occupies each tweezer. In the realization of the array no evaporative cooling procedure is needed, since the efficient Doppler cooling performed thanks to the red line is enough to trap the atoms in the optical tweezers, whose trap depth is on the order of 1 mK [15]. This allows to significantly reduce the be exploited to keep the atoms below a desired value of motional energy within the trap [33, 34].

Fluorescence imaging of the loaded array is then performed (while still cooling) to determine which tweezers contain an atom. Consequently, the rearrangement of the atoms into a desired configuration is carried out (as discussed in section 2.4), then the atoms are imaged again to verify the success of rearrangement, and cooled again. Only at this point, the actual "science" occurs. We can interrogate the clock transition or perform Rydberg excitation to induce entanglement between atoms, i.e. for quantum simulation experiments. Finally, state-selective detection operations and fluorescence imaging procedures are carried out, providing binary values that give information on the probability of occupation of the selected state and from which it is possible to extract information on the physics of the problem we are interested in.

4.3 The glass cell

The whole experiment takes place inside the glass cell, this avoids the transport of the cloud of cold atoms, making the setup as simple as possible and the experi-

mental cycle reduced. The cell and all the other components that surround it are made in such a way as to maximize the optical access to the atoms, necessary for MOT, imaging and tweezers beams. The cell is surrounded by a 3D printed plastic structure, assembled from two parts for optimum stability (figure 4.3), which can hold 8 rod-shaped electrode that are used to compensate stray electric fields.

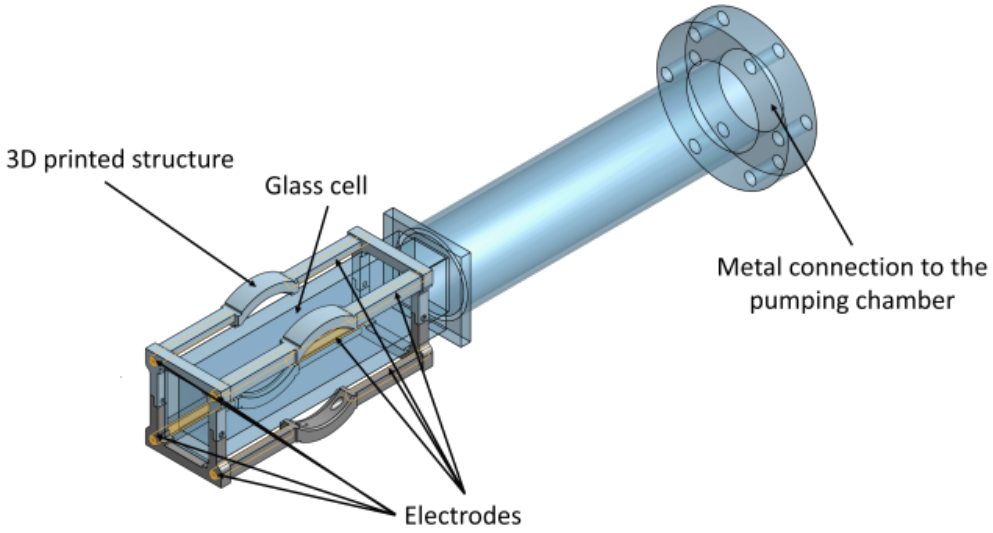

Figure 4.3: Rendering of the glass vacuum cell in which atom trapping occurs, surrounded by the 3D printed plastic structure with compartments where the electrodes for the electric field control are placed.

In addition to this plastic structure, the glass cell is also surrounded by other components required for the realization of the experiment, illustrated in figure 4.4. Two high-resolution objectives with high numerical aperture placed near the cell are responsible for both generating the optical tweezer arrays and for collecting fluorescence from the atoms. Two coils will be used for the generation of high magnetic fields, exploited both for the realization of the MOTs and for the excitation of the clock state. The geometry of the coils will be discussed in detail in chapter 5, devoted to the magnetic field simulations carried out for this thesis. The whole is surrounded by a further larger support structure where six smaller coils are placed, for tuning the position of the MOT, tuning quantization axes or compensating background fields.

The entire vacuum apparatus is designed to be as small and compact as possible

as it will be mounted on a translation stage. This would allow for future changes in the setup, or for any required maintenance, simply removing the chamber without any disturb for all the optical setup.

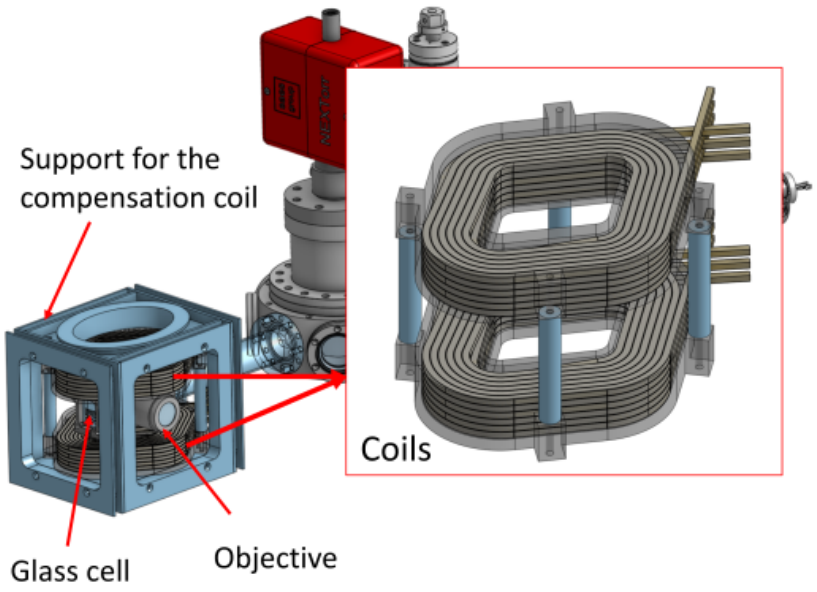

Figure 4.4: Glass cell with all the main surrounding components, including microscope objective, low-field and high-field magnetic coil with their support structure.

Chapter 5

Design of the high-field coils

For the realization of this experiment magnetic fields are important for several purposes, including the excitation to the clock state and the generation of the MOTs. In order to realize these fields in a controlled way, as already mentioned in chapter 4, in our experimental set up there are two sets of coils. The first is a set of three pairs of non-cooled low-field coils, which can produce small independent magnetic fields in all three directions. The second set is a pair of water-cooled coils for the generation of high magnetic fields.

In particular, in this chapter I present the simulations carried out with the COMSOL Multiphysics software for the design of the high-field coils.What is shown here is the final result of a series of simulations carried out by varying all the degrees of freedom available in the design of the coils, including the cross-section of the wire, the diameter of the hole inside the wire, the size of the coils, the number and arrangement of the windings. In the end, the optimum geometry was found, which is illustrated below.

The requirements that enter into the design of these coils are:

- The ability to produce magnetic fields of $> 500\,\mathrm{G}$ in one direction to achieve large Rabi frequencies on the clock transition, for bosonic strontium isotopes (see section 2.1).
- The ability to produce magnetic field gradients of at least $10\,\mathrm{G}$ / cm to ensure a proper operation of the blue MOT.
- A large degree of optical access to the atoms in the glass cell.

The coils have been designed in such a way as to ensure correct operation as regards both the generation of magnetic fields for the experiment, and an effective cooling of the coils themselves.

Figure 5.1 shows a drawing of the coils with the glass cell and the microscope objectives, which are placed between the two nearest opposite faces of the coils. The presence of the objectives imposes a lower limit on the distance between the two coils. Since the diameter of these objectives is 50 mm, all the simulations are carried out with a distance between the two nearest opposite face of the coils of 57 mm to ensure a 3.5 mm gap between the components.

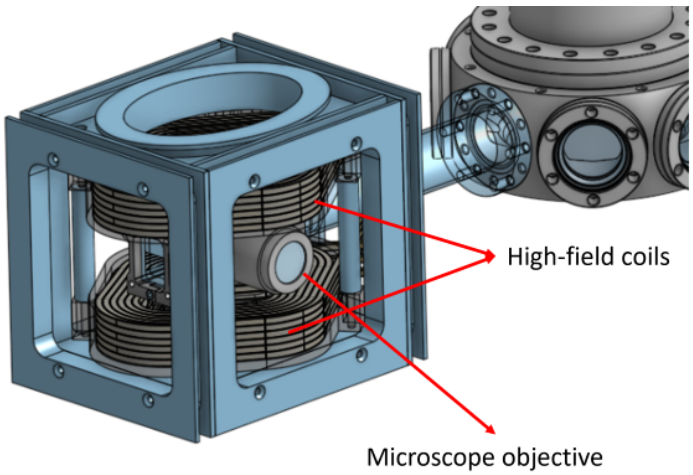

Figure 5.1: Picture of the glass cell surrounded by the high-field coils and the objective.

Beside the generation of magnetic fields, these coils must also guarantee a high degree of optical access to the atoms in the glass cell, that is why we have chosen a rhombus shape (inspired by the design in [15]) as it provides the best compromise for both the requirements. The shape design with the dimension of the coils, as obtained from the simulations described in this chapter, is illustrated in figure 5.2. Meeting the same requirements with traditional round-shaped coils would have made the system extremely bulky.

After a series of simulations carried out with different wire and winding configurations I have estimated that the best one, both for the magnetic field generation and for an efficient cooling of the coils, is the one in which each coil is made with 6x7 windings of hollow core copper wire.

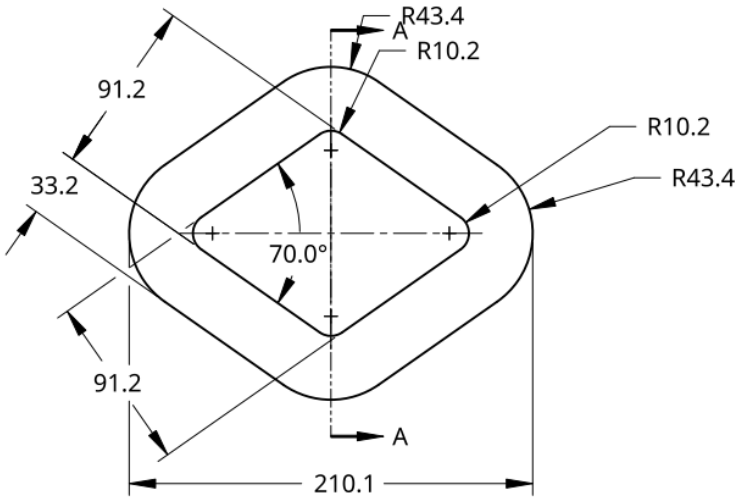

Figure 5.2: Shape and dimensions of one of the high-field coils (expressed in mm). The rhombus shape is the best compromise to maximize coil performance and optical access to the glass cell.

The operation of these coils generates a large amount of heat, which is a problem both because the system itself can be damaged and because it could bother with the realization of the experiment, heating the environment around the cell and i.e. compromising the imaging procedure. This heat must be dissipated and we have chosen to do it with a circuit of water flowing inside the coils, which led us to the choice of a hollow core wire. A possible alternative could have been to work with coils immersed in cooling tanks, but this would have made the system much more bulky and the installation of the coils themselves more challenging. The wire chosen for the realization of the coil has a rectangular section of 4 mm and a round hole with a diameter of 2.5 mm, as shown in figure 5.3. The cross section of the conducting part is $10.88\,mm^2$ and the hole area is $4.91\,mm^2$. Furthermore there will be a layer of insulator on the wire with a thickness of about $0.3\,mm$ (not shown in the figure).

The resistance of a conductor is directly proportional to the length and inversely proportional to the section, through the relationship:

$$R = \rho \frac{l}{s}$$

where l is the length of the conductor, s is the section of the conducting part and ρ is

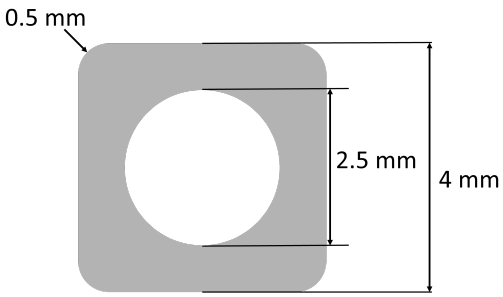

Figure 5.3: Cross section of the hollow core wire employed for the realization of the coils. The cross section of the conducting part is $10.88\,\mathrm{mm}^2$ and the hole area is $4.91\,\mathrm{mm}^2$.

the resistivity of the material, in the case of copper it is $\rho = 0.0175\,\Omega\frac{\mathrm{mm}^2}{\mathrm{m}}$. To make each of our coils we need about $18\,m$ of copper wire, which leads to a resistance of $29\,\mathrm{m}\Omega$ for each coil, in accordance with the results from the simulations. As they are mounted in series the total resistance will be $58\,\mathrm{m}\Omega$.

5.1 Magnetic field simulation

The simulations illustrated in this chapter were made by exploiting the Magnetic Fields interface (mf), under the AC/DC module, in the COMSOL Multiphysics simulation software, which solves Ampere's law for the magnetic vector potential. All the information about the interface can be found in [35].

The configuration of the coils and of the reference frame for the magnetic field simulation is illustrated in figure 5.4. The simulations were carried out in a cubic space with a side length of $5\,\mathrm{m}$, much greater than the size of the coils, to avoid boundary condition effects in the area where we are interested in simulating fields. The materials assigned, whose characteristics are already contained in the software database, were copper for the coils, quartz for the cell, and air anywhere else.

The calculation of the magnetic field produced in the module mf was carried out with the use of the Homogenized Multi-Turn Coil setting, which models a bundle of tiny wires tightly wound together but separated by an electrical insulator. The cross-section area of the individual wire in the bundle is user defined at $10.88\,\mathrm{mm}^2$, which is the section of the conducting part for the wire we chose. The selected number of turns was $N = 42$, this is the number of wires constituting the coil. The

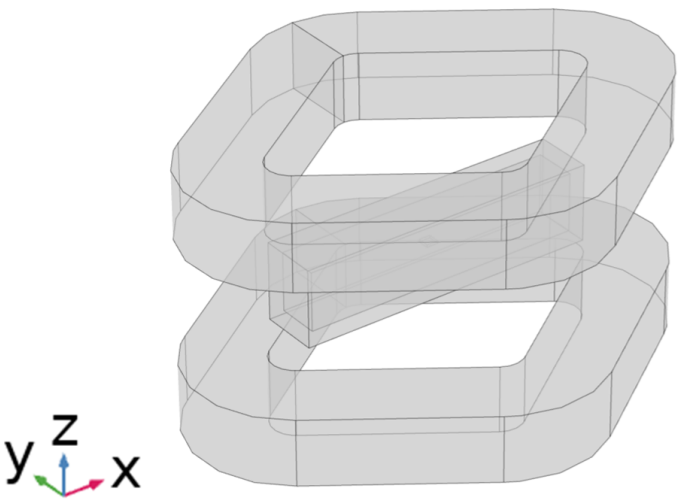

Figure 5.4: Configuration of coils employed for the simulation of magnetic fields both in Helmoltz and anti-Helmoltz configuration. Three orthogonal directions are defined for reference, the x axis which points along the long dimension of the glass cell toward the vacuum chamber, the y axis along the axis of the objectives and the z axis which is orthogonal to the first two axes. The origin of the reference system coincides with the midpoint between the two coils along their axis.

default value of the conductivity for copper is $6 \cdot 10^7\,\mathrm{S/m}$.

I have set as the charging source a current value of $I = 190\,\mathrm{A}$, which forces the total current flowing in the coil wire. The direction of current flow in this case is simulated by specifying the input boundary and the direction which is orthogonal to the interior boundary that crosses the wires chosen as inlet surface, as shown in figure 5.5. The consequent voltage drop for a resistance of $58\,\mathrm{m\Omega}$ is $11\,\mathrm{V}$, and the total power is about $2.1\,\mathrm{kW}$. The geometry of the wires and the current value have been chosen also considering the market availability of suitable power supplies. For the voltage-current characteristics of the final design it is convenient to use a DC Power Supply SM30-200 by Delta Elektronika, $0 - 30\,V\ 0 - 200\,\mathrm{A}$.

For the sake of simplicity, in the remainder of this discussion, we will call the Helmoltz configuration the one in which the current flows in the coils in the same direction, and the anti-Helmoltz configuration the one in which the current flows in the opposite direction in the two coils, without requiring specific conditions on the

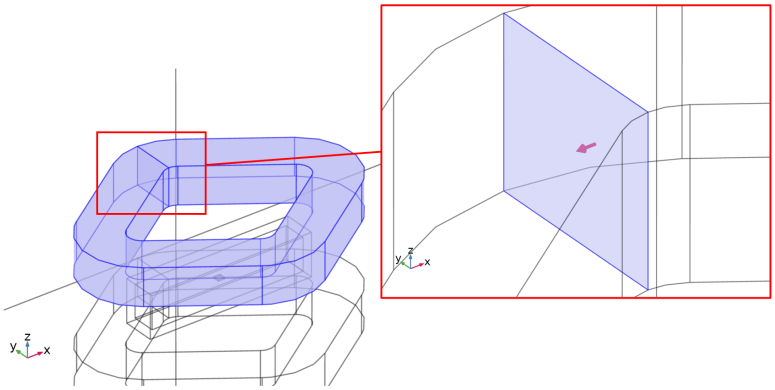

Figure 5.5: Interior boundary that crosses the coil used as an input boundary with the direction of the current.

cancellation of field derivatives as in the more specific meaning of the term. The results of the simulations for the coils operating in Helmoltz configuration, solved in the stationary model solution for a current $I = 190\,\mathrm{A}$, are shown in figures 5.7 and 5.6. We are able to obtain a magnetic field greater than 900 G at the center of our experimental system, that meets our demands. For bosonic ^{88}Sr atoms the Rabi frequency of the clock transition, induced by a static magnetic field B together with an optical field of intensity I is given by [18]:

$$\Omega = \alpha\sqrt{I}|B|$$

with $\alpha = 2\pi \times 198\,\frac{\mathrm{Hz}}{T\sqrt{\mathrm{mW\,cm^{-2}}}}$. With a magnetic field $B \approx 900\,\mathrm{G}$ and an intensity $I \approx 1\,\frac{\mathrm{W}}{\mathrm{cm}^2}$ the achievable Rabi frequency is $\Omega \approx 2\pi \times 560\,\mathrm{Hz}$ which guarantees sub-ms clock excitations (see section 2.1).

Similar simulations were carried out for the coils in the anti-Helmoltz configuration, with the only difference being the change of direction for the current flow in one of the two coils (changing the direction of the current in the input boundary). The results are shown in figures 5.9 and 5.8. A field gradient of 90 G/cm is obtained in the x direction, 125 G/cm in the y direction and 200 G/cm in the z direction. These values are well appropriate for the operation of the blue MOT.

Simulation of magnetic field with coils in Helmoltz configuration

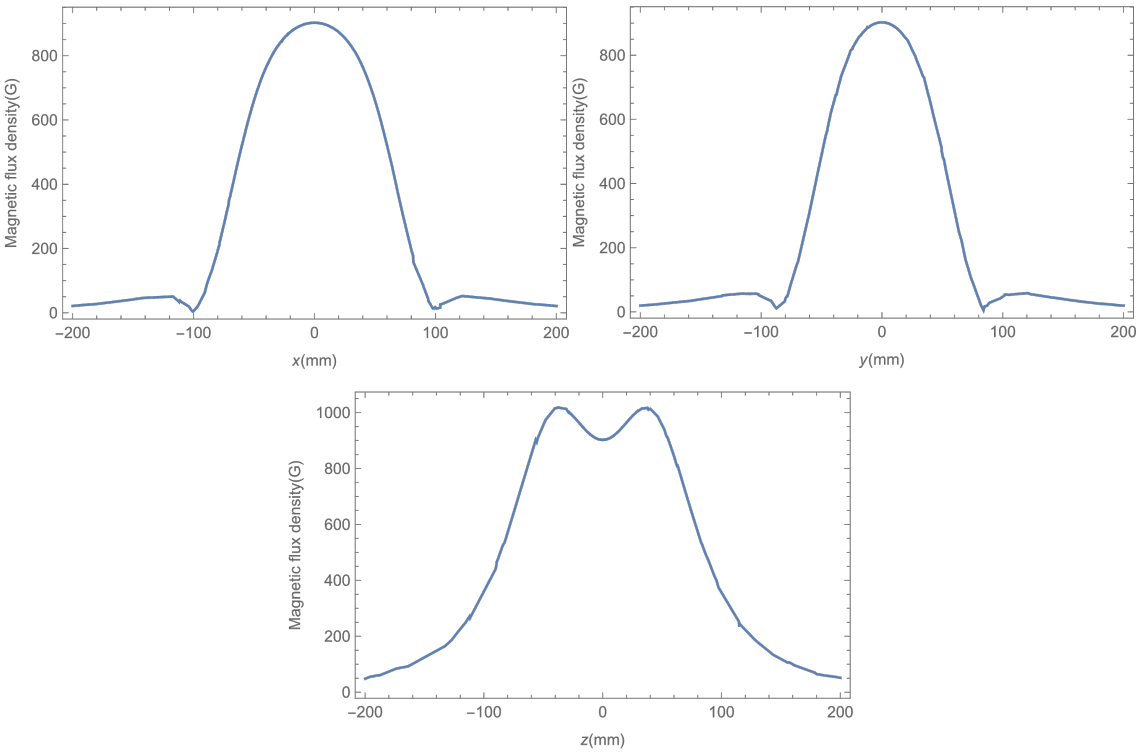

Figure 5.6: Magnetic density flux along the three directions for the coils in anti-Helmoltz configuration and a current $I = 190\,\mathrm{A}$.

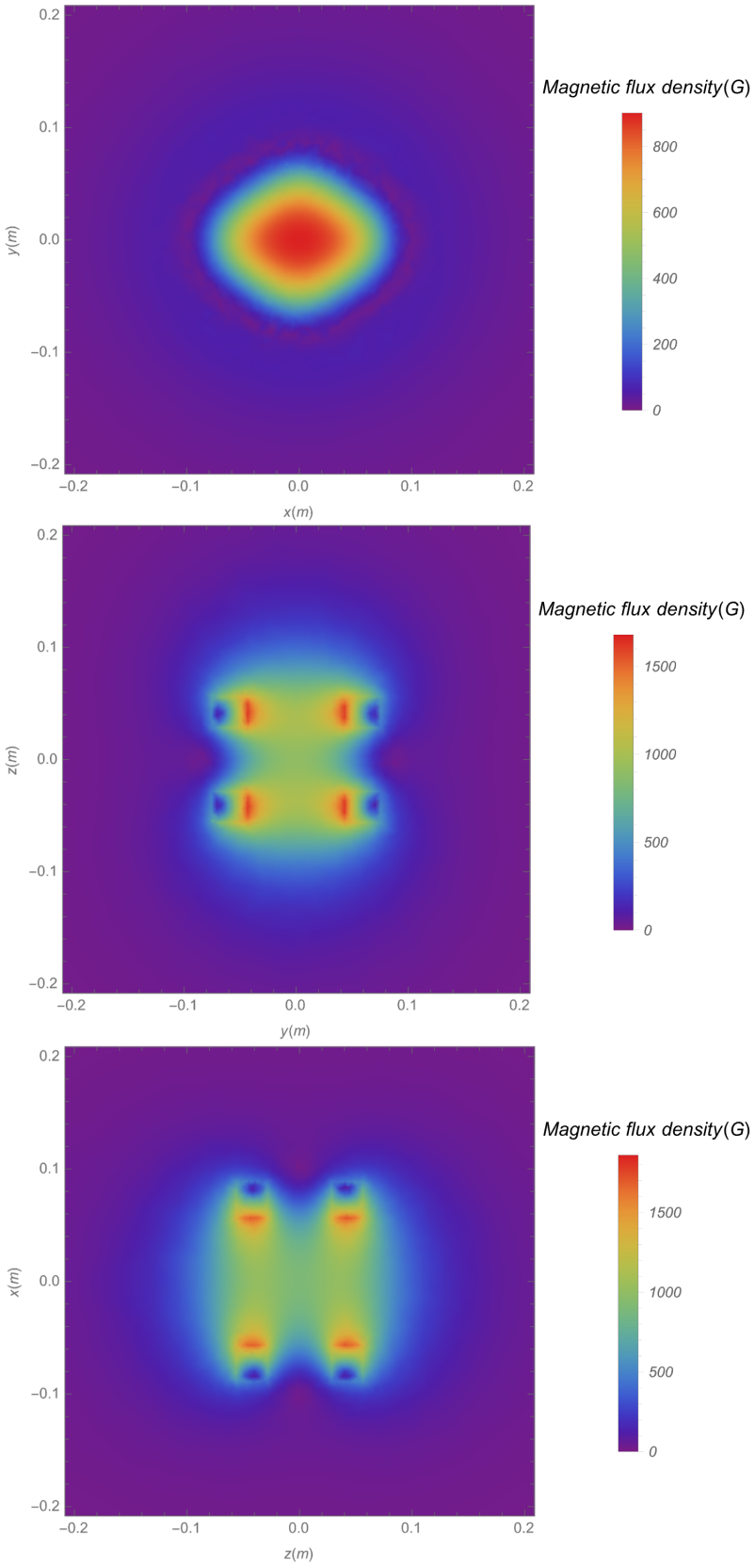

Figure 5.7: Magnetic density flux on x-y, y-z and x-z planes passing through origin for the coils in Helmoltz configuration and a current $I = 190\,\mathrm{A}$.

Simulation of magnetic field with coils in anti-Helmoltz configuration

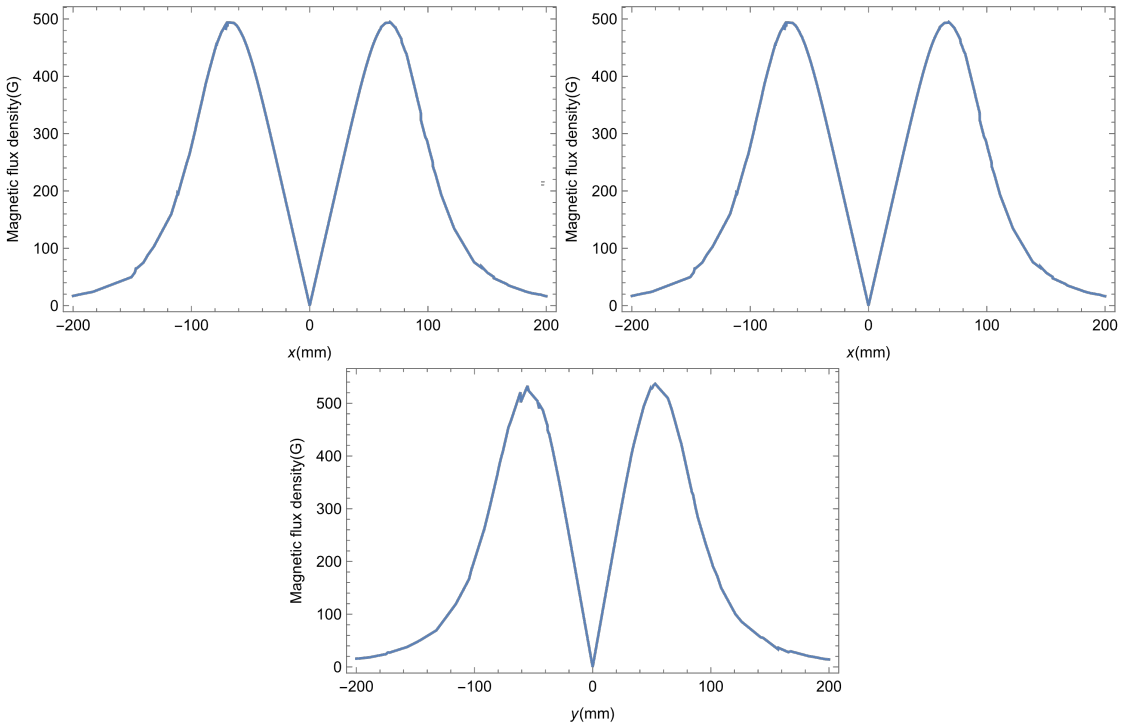

Figure 5.8: Magnetic density flux along the three directions for the coils in anti-Helmoltz configuration and a current $I = 190\,\mathrm{A}$.

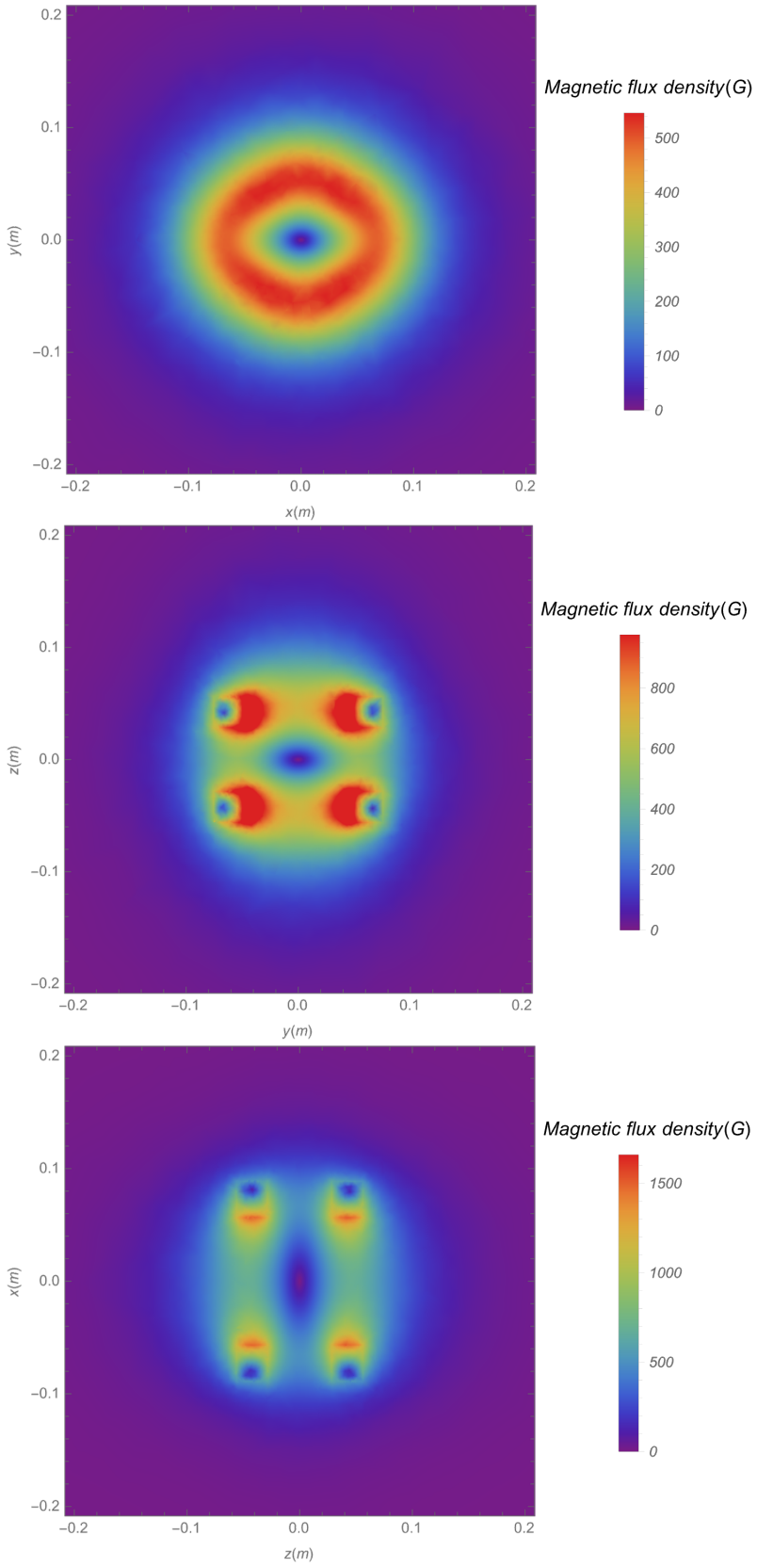

Figure 5.9: Magnetic density flux on x-y, y-z and x-z planes passing through origin for the coils in anti-Helmoltz configuration and a current $I = 190\,\mathrm{A}$.

5.2 Cooling simulation

As already mentioned, the issue of cooling is a fundamental aspect in the design of these high-field coils. The ability to properly dissipate the heat generated by the coils during their operation is crucial for the realization of the experiment. The flow of electricity through a conductor produces heat due to the Joule effect. Joule's first law states that the power of heating generated by an electrical conductor equals the product of its resistance and the square of the current:

$$P = R \cdot I^2$$

The study was conducted considering the coils always in operation with a constant current of 195 A, which we set as the maximum limit of working of our system. For a resistance of 58 mΩ this leads to a power of about $P = 2.2\,\mathrm{kW}$ to be dissipated. This study does not represent normal operating conditions, rather they refer to but an extreme limit of operation. During an experimental cycle we expect the coils to be in operation for about 10% of the cycle time, in the case of Helmoltz configuration, to excite the clock transition. While for the anti-Helmoltz configuration, for the generation of the MOTs, the coils are in operation for about 50% of the cycle time, and roughly half the current is flowing trough them. The simulations were carried out by pushing the coils to the their limits to verify that even the most critical operating situation can be sustained.

Our aim is to harness the water flowing inside the hollow core copper wire that makes the coils, to provide an effective cooling. To make the cooling more manageable with water chiller easily available on the market we have decided to split the cooling circuit. This was done in consultation with the manufacturer (OSWALD) to verify the actual possibility of realization. The cooling circuits are realized in parallel while the current circuit is instead in series.

The final design of the coil is illustrated in figure 5.10: each coil is divided into three parts each consisting of 2x7 windings. Furthermore, the coils are made with an external structure of epoxy resin which acts as a support for the coils themselves, allowing them to be assembled together with the other components of the setup.

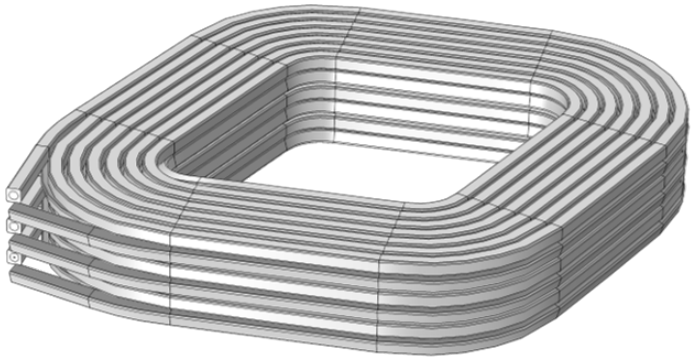

Figure 5.10: Rendering of the design of a single coil for the high magnetic field. The cooling circuit is realize splitting the coil in 3 parts consisting of 2x7 windings each.

5.2.1 Water flow in the coils

The general equation of motion for an incompressible Newtonian fluid is the Navier-Stokes equation [36]:

$$\rho\left(\frac{\partial \mathbf{u}}{\partial t} + \mathbf{u}\cdot\nabla\mathbf{u}\right) = -\nabla p + \rho\mathbf{g} + \mu\nabla^2\mathbf{u} \tag{5.1}$$

along with the continuity equation:

$$\nabla\cdot\mathbf{u} = 0 \tag{5.2}$$

where ρ and μ are the fluid density and viscosity, respectively, $\mathbf{u}$ is the velocity, p is the pressure and $\mathbf{g}$ is the gravity acceleration. Equation 5.1 is a highly non linear equation that consists of different terms. The term at left-hand side describes the bulk motion of our fluid; on the right-hand side we have the pressure gradient, the gravity force and then the viscous term. The pipe flow regime [37], which can be laminar or turbolent, is determined by the Reynolds number:

$$Re = \frac{\rho\bar{u}L}{\mu} = \frac{\bar{u}L}{\nu} \sim \frac{\text{inertial force}}{\text{viscous force}} \tag{5.3}$$

where $\bar{u} \equiv \frac{Q}{A}$ is the mean velocity, with Q the volume flow rate and A the cross section of the pipe and L is a characteristic length of the phenomenon considered: in the case of the motion of a fluid in a pipe, it corresponds to the pipe diameter.

The Reynolds number in equation 5.3 is an indication of the ratio between inertial force to viscous force. When $Re < 1$ the viscous force is actually dominating, which means that we can actually ignore the inertial effect. When $1 < Re \lesssim 2000$ the flow is in the laminar regime so the inertial force starts to become more important. As the Reynolds number continues to increase the inertial force dominates and that really contributes to the difficulty of the solving Navier-Stokes equation. Under normal conditions, the transition from a laminar to a turbulent regime occurs at $Re \approx 2300$ for flow in pipes. Turbulence occurs when the viscous forces in the fluid are unable to damp out random fluctuations in the fluid motion (generated, for example, by roughness of a pipe wall), and the flow becomes chaotic.

Now, if we think about a flow over a flat plate (figure 5.11) Re starts very small and continue to grow over the flat plate.

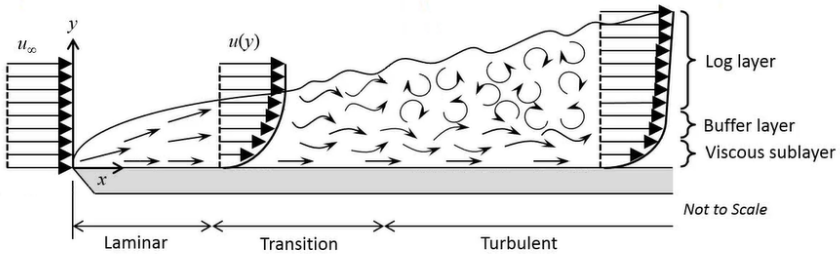

Figure 5.11: Scheme of the flow over a flat plate.

What we can see in the figure is the growth of a boundary layer. The flow starts being laminar and then it transitions to a different regime, where it becomes fully turbulent and causes a very chaotic behavior. Within the boundary region there are multiple layers: a log layer, a buffer layer and a viscous sublayer.

The laminar flow can be completely described by the Navier-Stokes equation, since the flow is very well behaved it does not vary too much in space or in time, so it can be resolved with a barely coarse mesh in the CFD module of COMSOL. As the Reynolds number increases the flow will start to oscillate in time and we cannot really solve a stationary problem any more, because a steady solution does not

exist, so we have to solve a time-dependent equation and with a finer mesh. Then, if the Reynolds number continues to increase, the flow becomes fully turbulent and exhibits more of a chaotic behavior and it starts to variate both in time and space. In this regime it doesn't even make sense to use $\mathbf{u}$, because the motion of the fluid is chaotic, instead we can use $\bar{\mathbf{u}}$ to represent the average velocity at a section along the pipe, that is subject to perturbations and that is what really makes turbulent flow difficult to solve. If we want to solve it directly with the Navier-Stokes equation we have to resolve all those small variations both in time and space, so we have to take a very fine mesh and solve it to a very tight time scale, but that is very computational-intensive and it can be solved in relatively small domains.

In our case, for water, with a density of $997\,\frac{\mathrm{kg}}{\mathrm{m}^3}$ and a viscosity $\mu = 1.002\,\mathrm{mPas}$, flowing in a 2.5 mm diameter pipe, the speed limit for the transition from laminar to turbulent regime ($Re = 2300$) corresponds to an average speed of about $0.8\,\mathrm{m/s}$ and a mass flow rate of $\approx 4 \cdot 10^{-3}\,\mathrm{kg/s}$. We will see later that higher mass flow rates will be required for our cooling process.
For this reason, the simulations were carried out considering a turbulent flow.

Given the very high complexity of the model to be simulated the COMSOL *Turbulent Flow* $k-\varepsilon$ (spf) interface is used mainly because of its low computational cost. $k-\varepsilon$ model has historically been very popular for industrial applications due to its good convergence rate and relatively low memory requirements. The equations solved by the *Turbulent Flow* $k-\varepsilon$ interface are the Reynolds-averaged Navier-Stokes (RANS) equations for conservation of momentum and the continuity equation for conservation of mass. This model is solved for two variables: k, the turbulence kinetic energy, and ε, the rate of dissipation of turbulence kinetic energy. All the information about the interface can be found in [38].

5.2.2 Heat exchange

Once the flow model inside the coils has been solved, it remains to calculate the heat exchange between the coils and the water.

The main heat exchange mechanism in our problem is the forced convection. This mechanism is described by the Newton's law for fluids:

$$q = hA(T_s - T_m) \tag{5.4}$$

This equation states that the rate of heat loss of a body (q) is proportional to the difference in temperatures between the body and its surrounding environment. In the above equation h is the convection heat transfer coefficient, A is the exchange surface (in our case the lateral surface of the pipe) and T_s and T_m are the temperatures of the coil and water, respectively. There is also a contribution of thermal conduction, described by the Fourier's law, that anyway is little with respect to the forced convection. The ratio between these two contributions is constant for a laminar flow and is defined as the Nusselt number [39, 40]:

$$Nu = \frac{\text{convective heat transfer}}{\text{conductive heat transfer}} = \frac{hl}{k} \tag{5.5}$$

where l is a typical length scale of the system (the diameter of the pipe) and k is the thermal conductivity of the fluid, approximately $0.6\,\frac{\text{W}}{\text{m·K}}$ for water at 20° C. In turbulent flows the Nusselt number is a function of the Reynolds number and the Prandl number:

$$Pr = \frac{\mu c_p}{k}$$
$$Nu = 0.023 Re^{0.8} Pr^{0.4}$$

where c_p is the specific heat capacity of water.
The Newton's law can be inverted to find the temperature of the coil given that of the fluid:

$$T_s = T_m + \frac{q}{hA} \tag{5.6}$$

The problem is now to find the temperature profile of the water inside the pipe. If we consider a constant power density dissipated by the coils, the energy balance calculated through a control volume gives us [41]:

$$\ddot{q}_s 2\pi r dx = Q c_p dT_m \;\Rightarrow\; \frac{dT_m}{dx} = \frac{\ddot{q}_s 2\pi r}{Q c_p} \tag{5.7}$$

where $\ddot{q}_s = \frac{q}{A}$ is the power density dissipated, r is the radius of the pipe, Q is the mass flow. Assuming that the power density is constant, the right side of the equation is independent of x, hence T_m is linearly dependent on the axial coordinate of the pipe:

$$T_m(x) = T_{in} + \frac{\ddot{q}_s 2\pi r}{Q c_p} x$$

and, using the relation 5.6 between surface and medium temperatures :

$$T_s(x) = T_{in} + \frac{\ddot{q}_s 2\pi r}{Qc_p}x + \frac{\ddot{q}_s}{h}$$

The plot of the temperatures as a function of the pipe's length is the following:

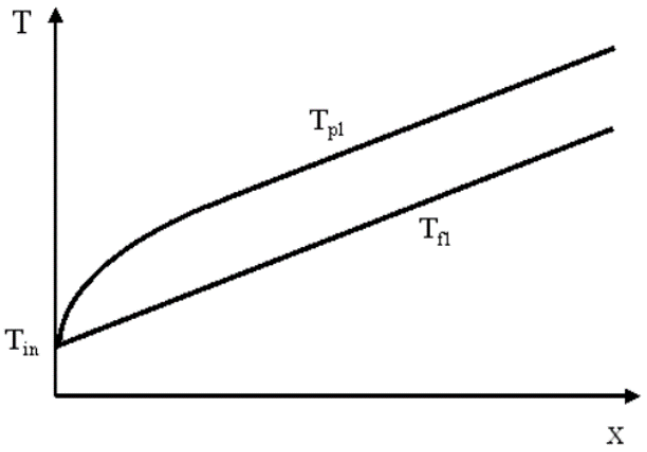

Figure 5.12: Wall temperature T_{pl} and fluid temperature T_{fl} as a function of the x-coordinate, which represents the pipe length, for convection with imposed heat flow. [41]

The surface temperature (T_{pl} in figure 5.12) has the same slope of the water temperature T_{fl} but the full developed regime is reached only after a distance that can be calculated to be :

$$x_{fd,t} = 0.05ReDPr \qquad \text{for laminar flow}$$
$$x_{fd,t} = 10D \qquad \text{for turbolent flow}$$

5.2.3 Results

As explained in the section 5.2, each coil consists of 6 planes with 7 windings each. To improve the performance of the cooling system, the coil was divided into three parts, each consisting of 2 planes. Given the complexity of the geometry and of the physics to be solved, including computational complexity, the simulations were carried out considering a single plane with 7 concentric windings illustrated in figure 5.13, instead of 2 planes which is the element of the cooling process. With

this configuration the resistance is about 4.84 mΩ, for a current of 195 A we have a voltage drop of 0.94 V and a power of about 184 W to be dissipated. Since the length of the wire in this case is about 3 meters, we can consider the flux inside it to be fully developed both for the turbulent flow and for the heat exchange, and extend this solution to the overall length of the systems to be cooled.

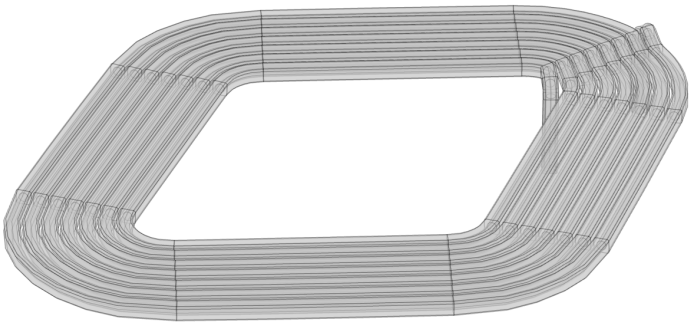

Figure 5.13: Scheme used for cooling simulations with a single plane with 7 windings.

The multyphysics interface of the software employed in these simulations allows to evaluate different physics models together, also taking into account that the water flow is non-isothermal.

The source of heating for the simulated element is taken directly from the previous simulation of magnetic field from the mf interface, while the cooling process is simulated within a heat exchange model that takes into account only the heat transfer between the heated wire and the water running inside with an initial temperature of 20 °C.

From previous simplest simulations it appeared that other heat exchange process between the coils and the enviroment, also taking into account the presence of the insulation layer sourrounding the wire, are negligible. Inserting the thermal transmission coefficient of the material in the space surrounding the windings or considering heat transfer between the system and the environment leads to a negligible correction in our system. So, for computational simplicity, I decided to proceed by taking into consideration only the heat exchange with the water flowing in the coils.

I have simulated the spatial evolution of the temperature of the conductor and the pressure drop of the water flux as a function of the water mass flow entering the circuit. The results are illustrated in figures 5.14 and 5.15, where the length on the horizontal axis represents the distance along the coil from the input point. These results are evaluated along a line that follows the geometry of the coils. Since the flux is numerically evaluated along a line rather than averaged over the conductor cross-section, the fluctuations that can be seen in the graphs could be attributed to the characteristic turbulence of the flux.

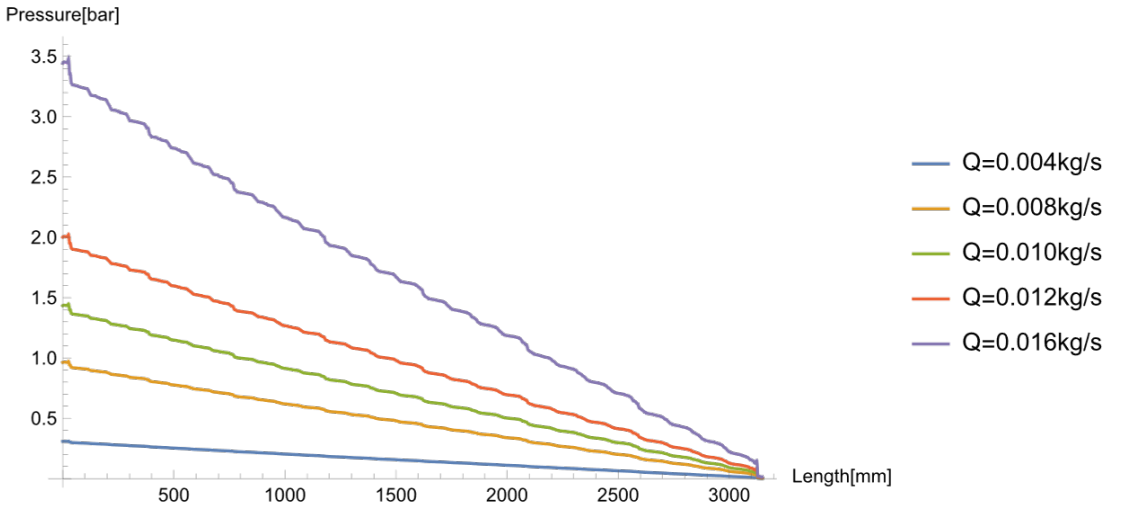

Figure 5.14: Pressure as a function of wire length for different water mass flow values for a coil with 7 wire windings.

From these simulations, we estimated that the optimum mass flow value to achieve a good compromise between coil temperature variation and pressure drop is $Q = 0.01\,\mathrm{kg/s}$, represented with the green lines in the previous graphs.

In the figures 5.16, 5.17 and 5.18 I report the simulation made for a flux of $Q = 0.01\,\mathrm{kg/s}$ mediated over the section of the conducting part for the copper wire and over the section of the hole inside the wire for the water (differently from the previous one which are evaluated just along a line). Excluding the initial and final parts of the simulated circuit, which are subject to edge effects, I estimated, performing some linear fit over those data, a change in temperature and a pressure

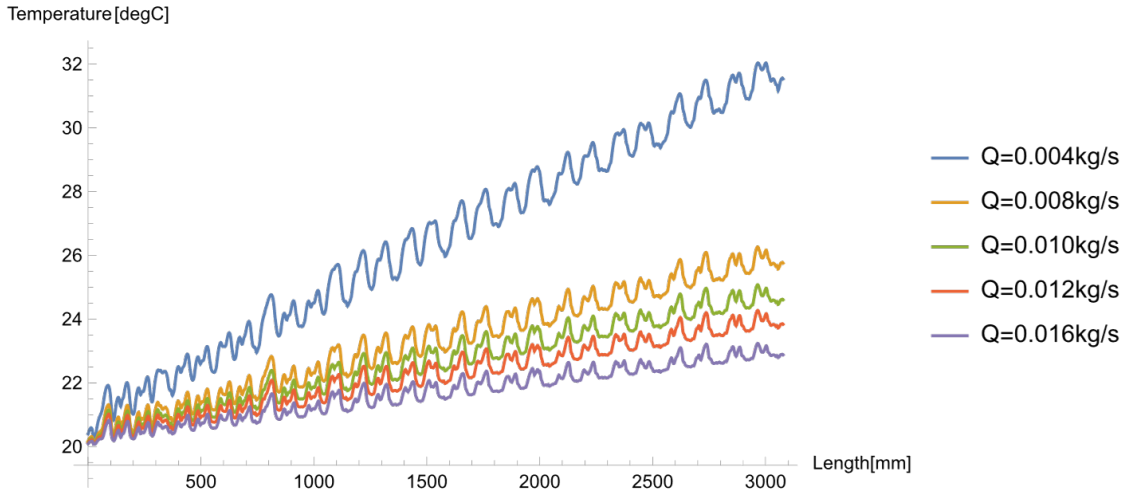

Figure 5.15: Temperature of the copper wire as a function of wire length for different water mass flow values for a coil with 7 wire windings.

drop of :

$$\Delta T = 1.4 \frac{^\circ\mathrm{C}}{\mathrm{m}}$$

$$\Delta P = 0.37 \frac{\mathrm{bar}}{\mathrm{m}}$$

Extending this result to the cooling component consisting of two planes with 7 windings, which is about 6 m we have a temperature increase of 8.4 °C in each one of the three sections in which the coil is splitted, which is acceptable, and a pressure drop of 2.2 bar. To this pressure drop other losses must be added, which are losses due to valves, elbows, and so on that are not considered in this simulation because they are small compared to the losses due to the friction in the pipe.

I would like to further emphasise that these simulations were carried out for critical operating conditions that we do not expect to occur in the normal operation of the experiment. They therefore represent an overestimation of what will actually happen.

Following the results of these simulations, we chose to use for the cooling system a chiller P30300 from Technotrans, which can dissipate a Power of 3000 W with a flow rate of 4.2 l/min at 3 bar, which is enough to ensure a proper cooling.

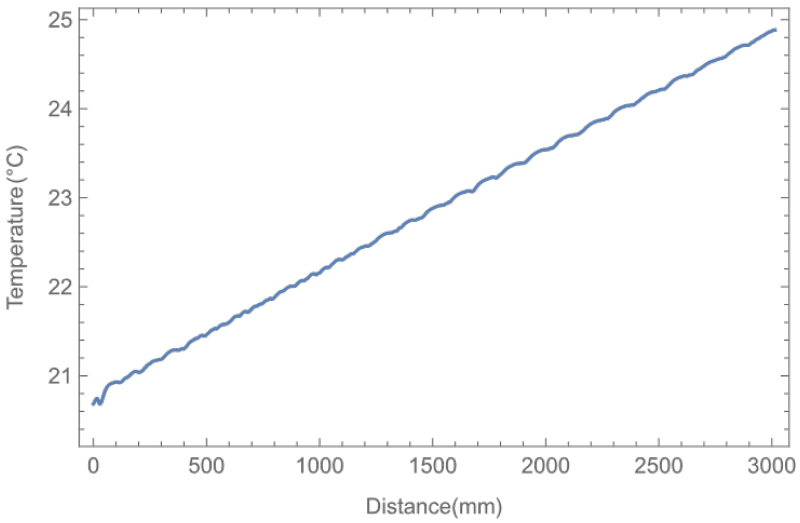

Figure 5.16: Mean temperature of the wire as a function of the distance from the inlet face for a mass flow of 0.01 kg/s, mediated over the section of the conducting part of the wire.

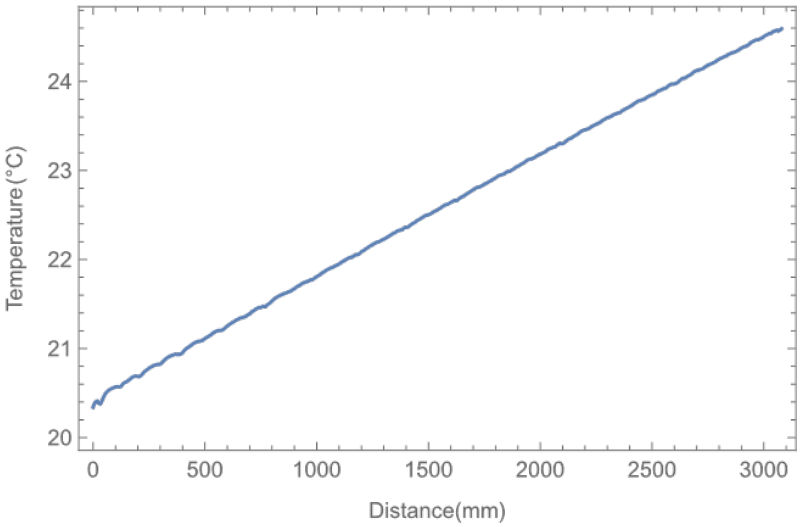

Figure 5.17: Mean temperature of the water as a function of the distance from the inlet face for a mass flow of 0.01 kg/s, mediated over the section of the hole inside the wire.

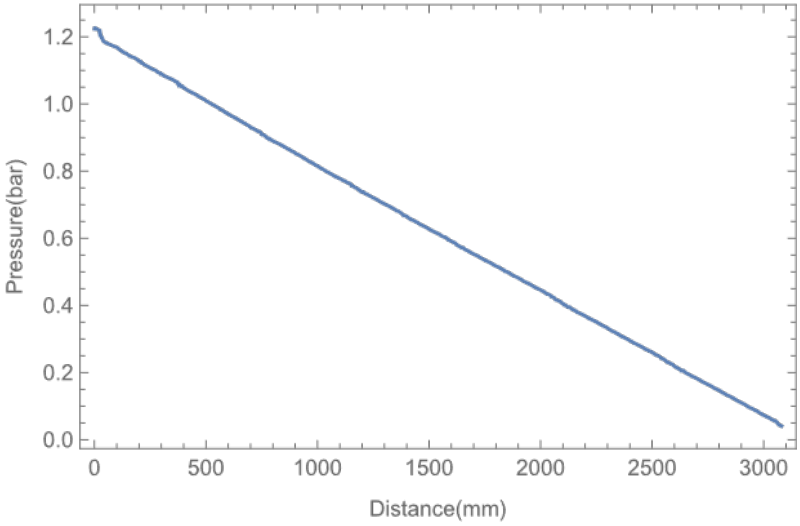

Figure 5.18: Mean pressure of the water as a function of the distance from the inlet face for a mass flow of 0.01 kg/s, mediated over the section of the hole inside the wire.

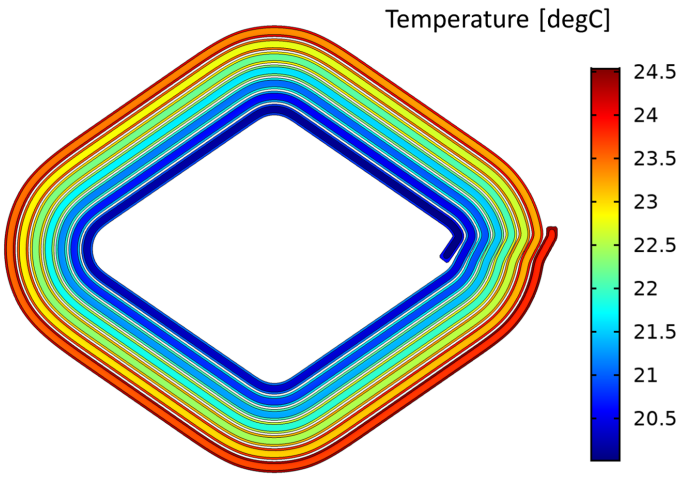

Figure 5.19: Bidimensional map of the temperature change in the plane perpendicular to the z axis that cuts the coils in half, for a mass flow of 0.01 kg/s.

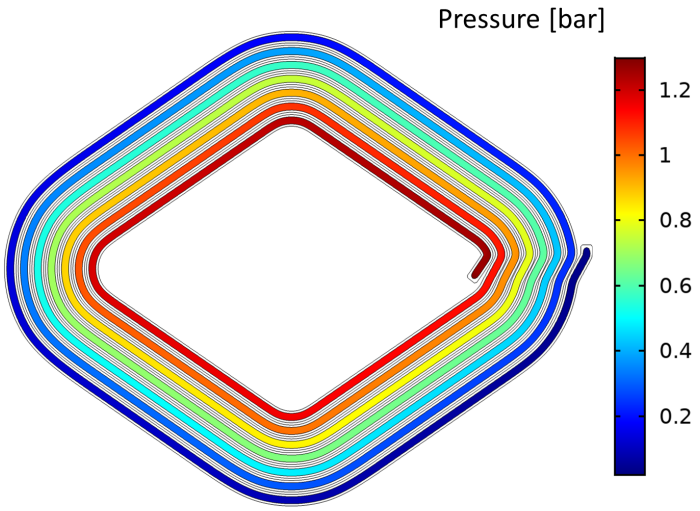

Figure 5.20: Bidimensional map of the pressure change in the plane perpendicular to the z axis that cuts the coils in half, for a mass flow of 0.01 kg/s.

Chapter 6

Measurements and results

In this chapter I present the measurements acquired and the relevant analyses carried out on the blue and the red laser sources and on the atomic source. The setups and measurements were carried out entirely by me during my thesis work. This results reported here represent a necessary step towards the realization of the experimental apparatus.

6.1 Blue laser

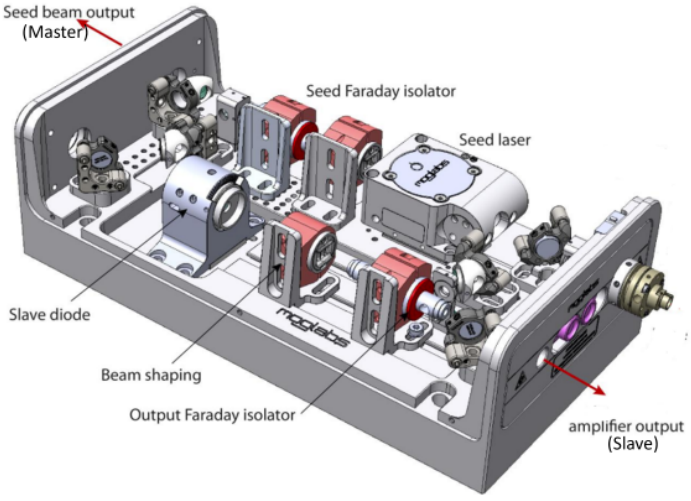

Figure 6.1: Picture of the injection-locked amplifier laser with its main components. The mirrors near the master output are used to adjust the alignment for injecting the seed into the amplifier.

The blue laser employed in the experiment (shown in figure 6.1) is an injection-locked laser system from Moglabs. The operating principle is to inject a small amount of light from a master laser, which is an external cavity-diode laser (ECDL) system built in the Littrow configuration [42], into a slave injection-locked amplifier (ILA), to force the latter to emit light in the same frequency mode as the master laser [43]. This technique increases the ability to obtain high power at the desired frequency, in our case 461 nm, compared to what would normally be emitted by a single ECDL.

The light generated by the master laser that is not used for the injection locking is emitted by a secondary laser output port and is employed in the experiment. The typical power obtained from the output of this laser is about $150\,mW$ from the master and $700\,mW$ from the slave at $461\,nm$. The slave output is split into four parts to provide light for the Zeeman slower ($\approx 375 - 400$ mW), 3D MOT (≈ 150 mW), imaging (≈ 10 mW) and imaging in tweezers (≈ 50 mW). The master output is used for the two 2D MOTs (≈ 125 mW) and for the stabilization of the laser on an atomic transition of strontium (≈ 10 mW).

The plot in figure 6.2 shows the power emitted by the master diode laser, stabilized at 20 °C, as a function of the current.

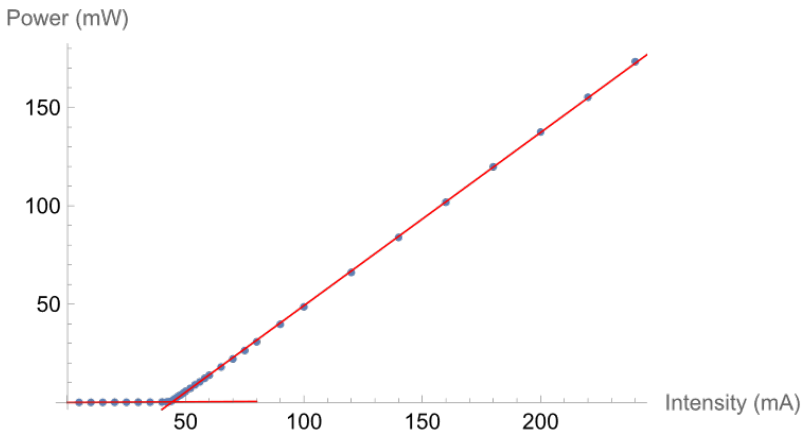

Figure 6.2: Power of the master diode laser ($T = 20\,°C$) as a function of the current. The blue dots represent the data recorded with a power meter, the red lines are the linear fit performed below and above threshold. The threshold current is 44.4 mA.

From the linear fit performed on the acquired data (also shown in figure 6.2) it is possible to derive the value of the threshold current that is 44.4 mA and a $0.880 \pm 0.002\,\frac{\text{mW}}{\text{mA}}$ slope efficiency above the threshold. We typically operate the

master laser around 220 mA to derive a power of about 150 mW.

A part of the optical setup for the master output of the blue laser is shown in figure 6.3.

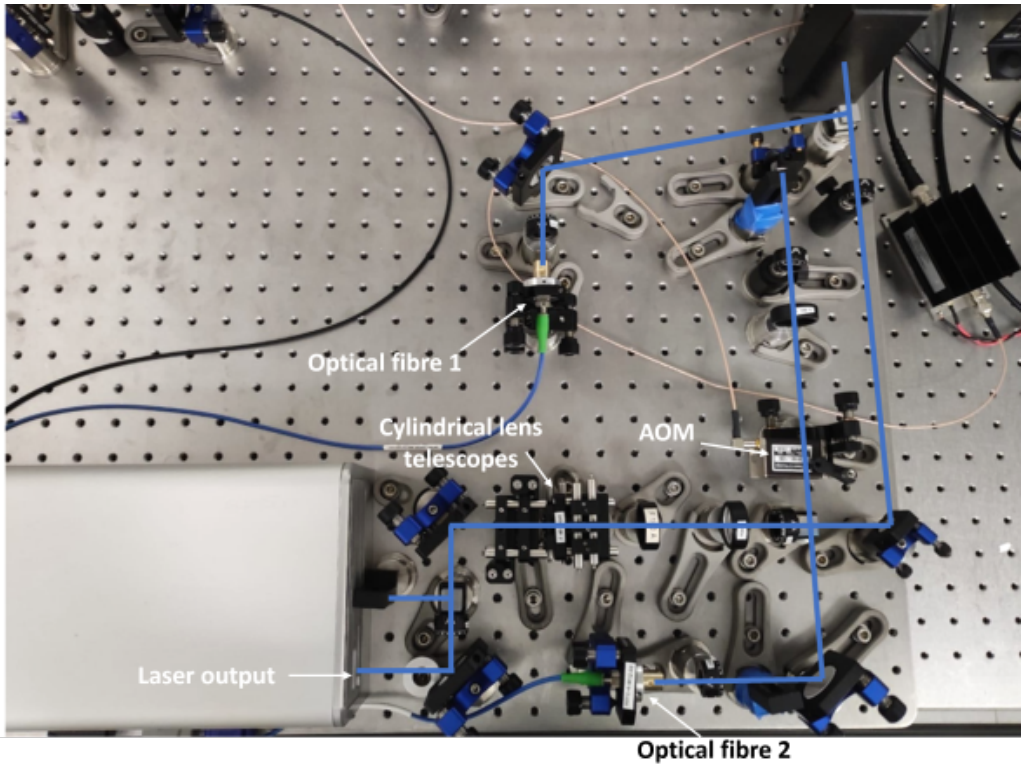

Figure 6.3: Picture of the optical setup for the master output of the blue laser.

The beam output of the master laser has a cross-section that is not circular but elliptical, in the horizontal direction it measures approximately twice as much as in the vertical direction. In figure 6.6 on the left we show a picture of the cross section of the laser beam at a distance of 16 cm from the laser output window.

The simplest solution to Maxwell's equations for representing a propagating laser beam is represented by a TEM00 Gaussian beam [48]. The corresponding intensity profile is:

$$I(r,z) = \frac{2P}{\pi w^2(z)} e^{-\frac{2r^2}{w^2(z)}} \tag{6.1}$$

where r=$\sqrt{x^2+y^2}$ is the radial coordinate and z is the axial coordinate. P is the power of the laser beam. $w(z)$ is the $\frac{1}{e^2}$ size of the laser beam at coordinate z along the propagation axis (illustrate in figure 6.4), which is a function of the beam waist

w_0, waist position z_0 and of the z_R Rayleigh length:

$$w(z) = w_0 \left(1 + \left(\frac{z - z_0}{z_R}\right)^2\right)^{\frac{1}{2}} \tag{6.2}$$

$$z_R = \frac{\pi w_0^2}{\lambda} \tag{6.3}$$

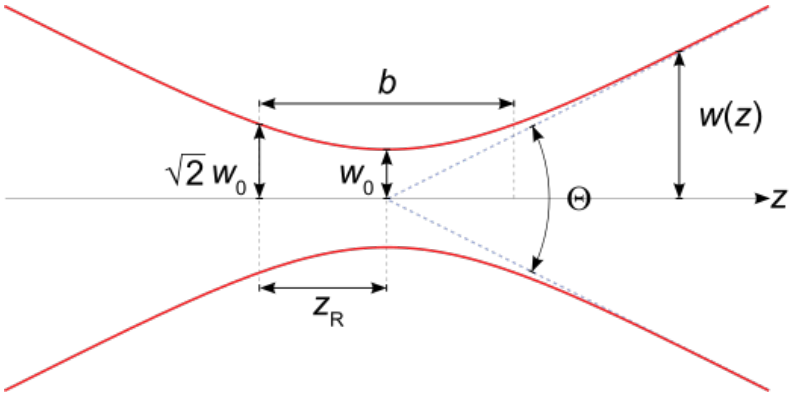

Figure 6.4: Gaussian beam width $w(z)$ as a function of the axial distance z.

In figure 6.5 some measurements of $w(z)$ are reported as a function of the distance from the laser output window with a fit with a Gaussian beam propagation function. These measure are obtained using a CCD camera placed at different positions along the beam, and fitting the images with a Gaussian to derive $w(z)$. The results of the fit are reported in table 6.1.

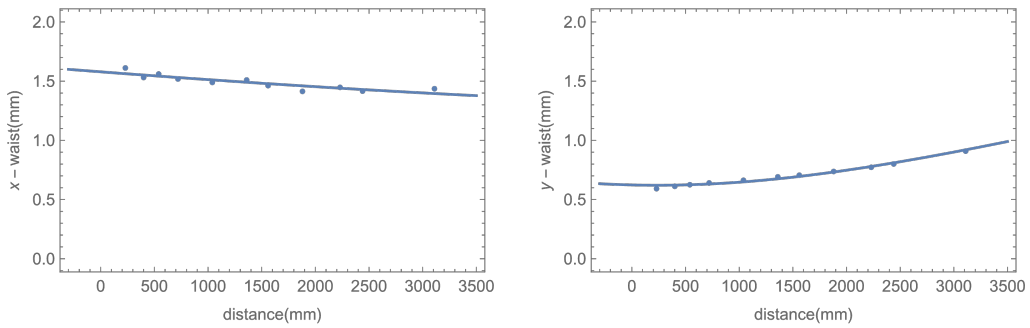

Figure 6.5: Measured w(z) for the master laser along the transverse x and the y direction, as a function of the distance is taken from the laser output window. The line is a fit to equation 6.2.

	w_0 (mm)	waist z_0 (mm)
x-waist	1.27 ± 0.06	8119 ± 540
y-waist	0.62 ± 0.01	237 ± 48

Table 6.1: Dimension and position of the waist of the master laser, the position value refers to the distance from the output window of the master laser.

In order to obtain a cross-section as circular as possible, a pair of cylindrical telescopes was introduced in the setup at the laser output. The first telescope consists of two cylindrical lenses, the first with focal length $F = 40\,\text{mm}$ and the second $F = 25\,\text{mm}$, that reduce the horizontal dimension. The second is made from two lenses with the same focal lengths as the previous ones but with inverted positions and rotated by 90 degrees, that increase the vertical dimension of the section of the beam. The shape of the beam after the two telescopes (18 cm far from the last telescope lens) is shown in figure 6.6 right, it has a rounder shape with a waist of about 1 mm.

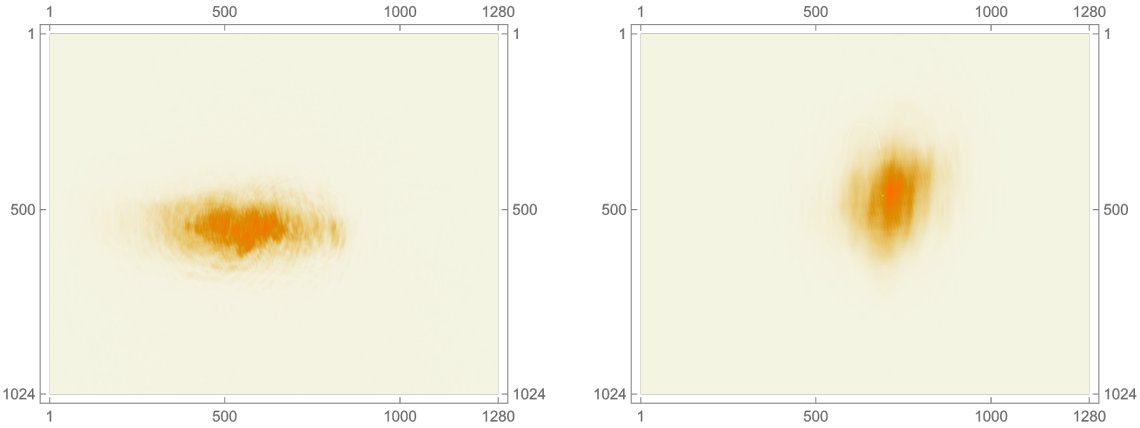

Figure 6.6: Picture of the section of the laser beam before (left) and after (right) the cylindrical telescopes obtained using a CCD camera. The units on the horizontal and vertical axes are given in camera pixels, each pixel measuring $5.2\,\mu$m

After the cylindrical telescopes the beam passes through another telescope consisting of two spherical lenses with focal lengths respectively $F = 100\,\text{mm}$ and $F = -50\,\text{mm}$, 5 cm apart, to further halve the beam size all the way through. The beam is then splitted in two parts by a beam splitter (BS). One part, used to perform spectroscopy on the windows near the oven to check the operation of the source, is injected into fiber 1 (this part of the setup is temporary). The other part of the beam is used to perform spectroscopy on the small window near the hot window and to stabilize

the laser frequency on the atomic transition ${}^1S_0 \rightarrow {}^1P_1$ of strontium. This beam undergoes a double pass through an AOM modulated at +117 MHz with an efficiency of around 60% and is then coupled into fiber 2 with an efficiency of about 30%.

6.2 Spectroscopy measurements

In order to obtain the following measurements, the first step is to bring the laser frequency as far as possible around the frequency of the transition interest (${}^1S_0 \rightarrow {}^1P_1$ at 460.82 nm), by manually changing the laser parameters (acting on the piezoelectric transducer voltage which controls the length of the Littrow cavity of the diode laser). A frequency scan is then enabled, by sending a periodic ramp signal to the piezoelectric. This allows the laser emission frequency to be varied in a controlled way over a limited range of frequency.

The technique used is absorption spectroscopy, which measures the absorption of radiation as a function of laser frequency due to the interaction with the sample. The measurements are performed with the laser beam propagating normal to the atomic flux. The signal intensity, with its variations due to absorption, is detected by a photodiode and converted into a voltage signal that is read on an oscilloscope as a function of time.

Both accesses provided by the atomic source manufacturer were used to perform spectroscopy measurements. The larger windows near the oven were used to test the proper operation of the atomic source, while the smaller windows near the hot window allowed more accurate spectroscopy measurements to be made. It was possible to carry out a calibration of the frequency scale by exploiting the known isotopic shift between strontium isotopes ^{86}Sr and ^{88}Sr, which are clearly distinguishable in this second set of measurements. This spectroscopy is also used to generate the error signal to stabilize the laser frequency.

Figure 6.7 illustrates the optical setup around the atomic source with the two fiber output sand the two spectroscopy schemes.

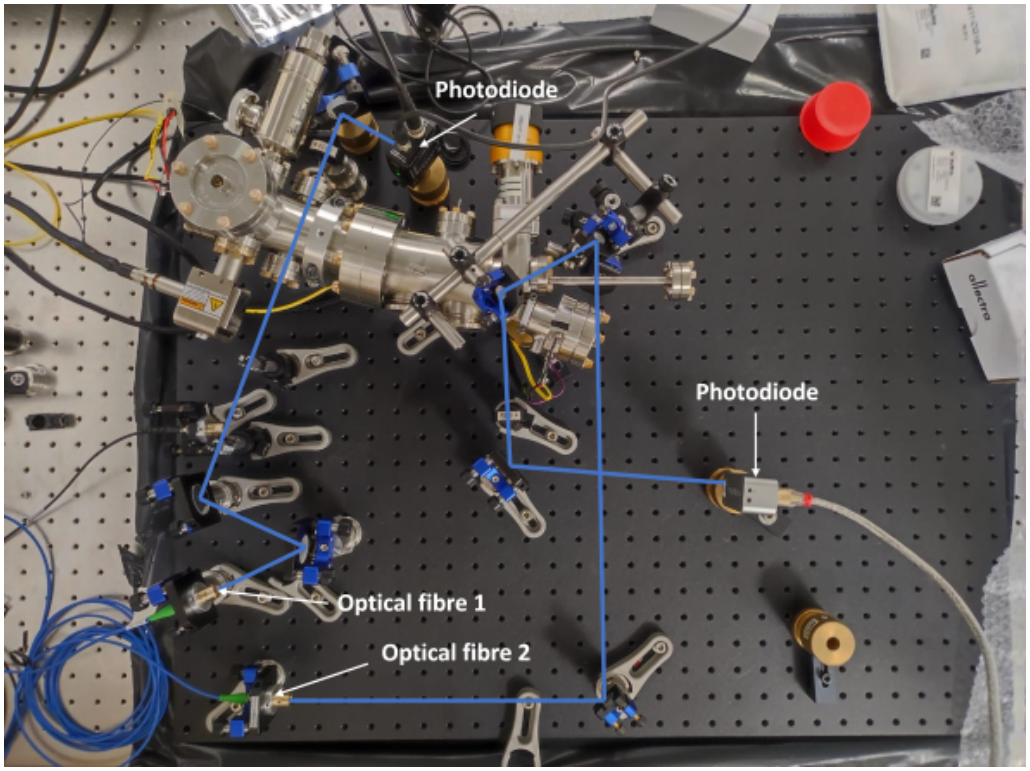

Figure 6.7: Picture of the optical setup around the atomic source for the spectroscopy measurements.

6.2.1 Calibration

At the time of the measurements we did not have access to an accurate wavelength meter, nor to a Fabry-Perot interferometer suitable for our wavelength range. Therefore, we had to resort to the known features of the Sr spectrum, primarily the isotope shift, to perform a frequency calibration of the spectra. Figure 6.8 shows a typical absorption spectrum (relative absorption) from the small spectroscopy windows, from which the photodiode background has been removed. Two different isotopes can be distinguished in this spectrum, ^{86}Sr and ^{88}Sr. The natural linewidth of this transition in about 32 MHz. In table 6.2 literature values for the Sr isotope shift are reported.

	^{84}Sr	^{86}Sr	^{87}Sr	^{88}Sr
$^1S_0 \rightarrow {}^1P_1$ shift	-270.8	-124.8	-45.6	0

Table 6.2: Isotope shifts of the Sr isotopes, given in MHz. All values are referenced to the most abundant isotope ^{88}Sr [44].

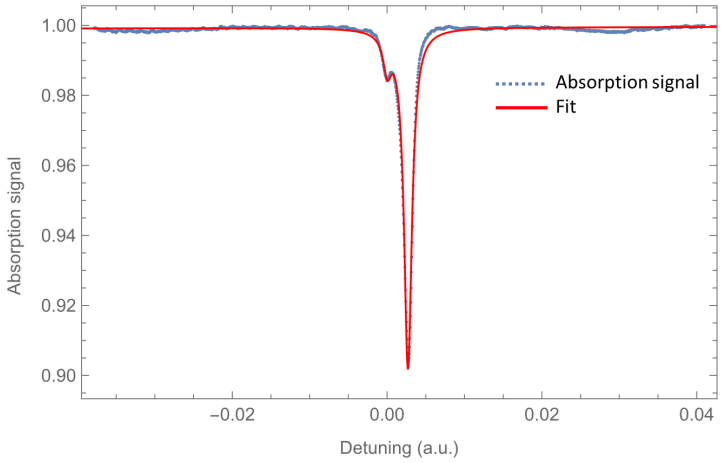

Figure 6.8: Absorption spectrum of the $^1S_0 \rightarrow {}^1P_1$ transition of strontium from the small spectroscopy window, with the oven at 500 °C. The red line is the lorentzian fit.

Given the known values of the energy shifts for the different isotopes, it is clear why to assign ^{88}Sr and ^{86}Sr to the two peaks of our signal. ^{88}Sr is the most abundant isotope and represents the biggest peak. ^{87}Sr is too close to ^{88}Sr to be distinguishable in this signal (the isotope shift is only 40% larger than the natural linewidth) and the line would be split in three weaker hyperfine components. and ^{84}Sr is not only further away, but also significantly lower in abundance than the others and therefore also not visible in the signal.

I acquired these spectra changing the oven temperature from 420 °C to 500 °C in steps of 10 °C. In general, the spectrum will show lines characterized by both homogeneous broadening, due to power broadening, and non-homogeneous broadening, due primarily to the Doppler effect in the beam propagation direction. In an atomic beam, Doppler broadening is not described by a functional form known beforehand (because it will depend not only on the temperature of the source, but also on the way the atomic beam is collimated in the specific setup). As suggested by the spectra in figure 6.8, where isotopic shifts of about 100 MHz can be appreciated, we therefore assume - and then verify a posteriori - that Doppler broadening contributes less to the width of the lines, so we fit with a Lorentzian line profile as the effective line shape. For each spectrum I performed a fit with the sum of a

constant term, a linear function and two Lorentzian functions:

$$f(x) = M + Ax + B_1 \frac{G_1}{\pi} \frac{1}{G_1^2 + (x - x_1^2)} + B_2 \frac{G_2}{\pi} \frac{1}{G_2^2 + (x - x_2)^2} \tag{6.4}$$

For each spectrum I then derived the distance between the two peaks in the arbitrary units provided by the oscilloscope, averaged these values over the different measures of signal absorption and derived the error as the mean square deviation. I then assigned the separation thus obtained the value of 124.8 MHz, which is the known isotopic shift for this transition between the two isotopes. I thus obtained a calibration for the frequency scale with an accuracy of $\sim$ 1.4%, determined the fit error on the peak position (the uncertainty on the fitted separation is $\sim$ 1.8 MHz). I was then able to rescale all subsequent measurements, taking care not to change the laser scan during the acquisition.

6.2.2 Spectroscopy near the oven

The spectroscopy windows near the oven provide a way to test the performance of the oven itself. When the system will be fully operational (Zeeman slower included), these windows will allow observation of the uncooled atomic beam exiting the oven. The range over which the oven can be operated with practical values of hot atom flux is from 400 °C to 500 °C, which corresponds to a flux between $1.5 \times 10^{12} \frac{\text{atoms}}{\text{s}}$ to $8.2 \times 10^{13} \frac{\text{atoms}}{\text{s}}$.

The absorption spectroscopy measurements are illustrated in figure 6.9. These spectra are taken from the bigger spectroscopy windows at approximately 10 cm of distance from the oven. We observe that the linewidths are much larger than those measured at the smaller windows, therefore we argue that they reflect the transverse velocity distribution of the atomic beam. This distribution was not evident in the spectra discussed in the previous section because of additional atomic beam collimation stages between the two windows, leading to an enhanced velocity filtering along the transverse direction. The velocity distributions have a triangular-like shape, a characteristic of the collisionless regime inside the nozzle micro tubes [45]. It is possible to see clearly how the absorption increase with the temperature. The percentage of absorption, evaluated by deriving the minimum value of the normalized absorption peak, varies with temperature as shown in Table 6.3. These values

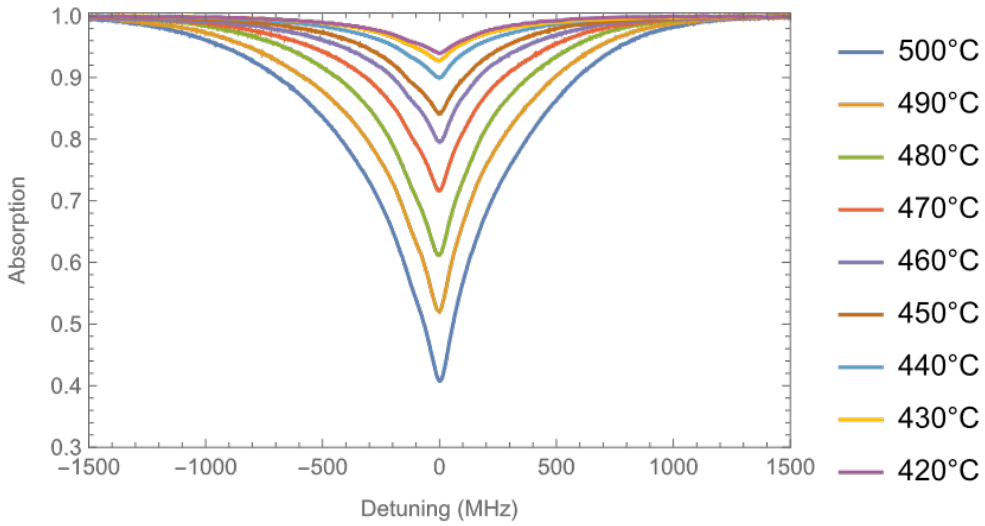

Figure 6.9: Absorption spectroscopy signal as a function of detuning acquired at the windows near the oven as the oven temperature changes.

for the absorption are characteristic of a good operation of the source according to the manufacturer.

Temperature °C	Absorption %
420	6
430	7
440	10
450	16
460	20
470	28
480	39
490	48
500	59

Table 6.3: Percentage of absorption as oven temperature changes.

Furthermore, during the acquisition of these spectra, we noticed some variations in the spectra as the polarization of the incident laser beam changed. We attributed this effect to the presence of a residual magnetic field from the permanent magnets of the Zeeman slower that shifts the m_F levels of the $^1P_1$ state. When the spectroscopy beam is linearly polarized along the atomic beam propagation direction (the same direction as the Zeeman slower magnetic field) the beam is π-polarized and drive the $m_F = 0 \rightarrow m'_F = 0$ transition. When the polarization is circular,

since the spectroscopy beam is normal to the stray magnetic field, we have a linear combination of σ^+ and σ^-, and the two stretch transitions $m_F = 0 \rightarrow m'_F = \pm 1$ are driven. When the polarization is elliptical we have both $\sigma^\pm$ and π. These spectra are illustrated in figure 6.10.

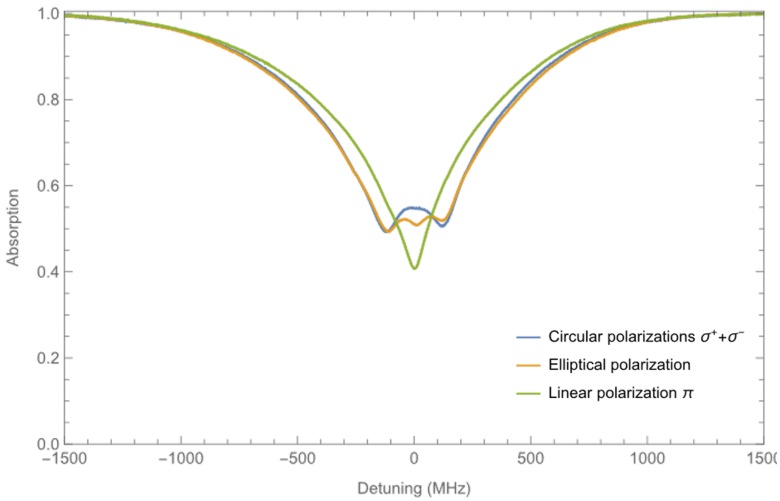

Figure 6.10: Absorption spectroscopy measurements as a function of detuning acquired at the windows near the oven changing the polarization of the incident beam.

The distance between the central peak and the two lateral peaks is about 120 MHz, and we can use this energy shift to calculate the value of the magnetic field at the point where the measurement is made. Since the Zeeman shift is

$$\Delta E = \mu_B B m_{F_e}$$

with $\mu_B = 9.27 \times 10^{-21} \frac{erg}{G}$, we obtain a magnetic field of about 86 G.

6.2.3 Spectroscopy near the hot window

Compared to the previous spectra, the measurements illustrated in this section, taken from the smaller windows near the hot window, have a much cleaner signal, as they are far from the permanent magnets and there are not much stray fields (apart from the earth one) and the atomic beam is more collimated.

The transition ${}^1S_0 \rightarrow {}^1P_1$ of ^{88}Sr has a linewidth $\Gamma = 2\pi \times 32$ MHz and a saturation intensity of $42.5 \frac{\text{mW}}{\text{cm}^2}$ [46]. These spectra are taken sending on the atoms

a laser beam with a waist of 1 mm and a power of 260 μW. The spectra acquired for different values of the oven temperature are shown in figure 6.11.

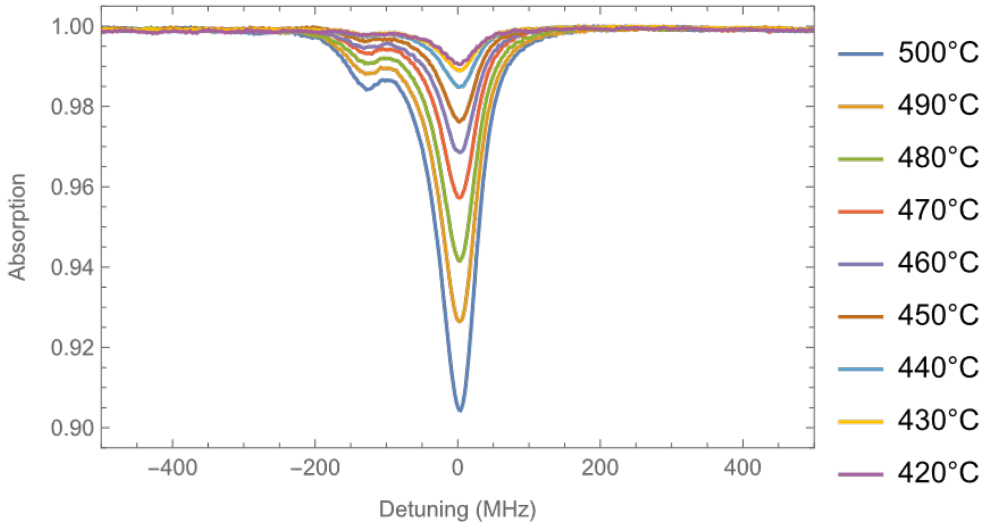

Figure 6.11: Absorption spectroscopy signals as a function of detuning acquired at the windows near the hot window for different values of the oven temperature.

The two absorption peaks of the two isotopes are clearly visible at all temperatures, although the peak of isotope ^{86}Sr becomes much more evident at higher temperatures beacause of the higher signal-to-noise ratio. It is possible to note how the signal increases as the oven temperature rises as a result of an increase in the atomic flux. As already mentioned, these spectra are much narrower and cleaner than the previous ones, denoting the presence of a more collimated beam. This is due to the geometry of the internal structure of the atomic source. The atoms arriving in this zone are in fact selected in the direction of propagation by the presence of narrow channels, which were not yet crossed when the spectroscopy was performed immediately outside the oven. In fact, the absorption signal for equivalent oven temperatures is much weaker in this case than in the previous one, thus also denoting the presence of far fewer atoms in the analysed region.

The Full-Width-Half-Maximum (FWHM) of the ^{88}Sr absorption spectra illustrated in figure 6.11 ranges from 50 ± 2 MHz to 58 ± 2 MHz as the temperature of the oven changes. This broadening of the spectrum may be due to several factors. The measurement is made with a laser beam perpendicular to the direction of propagation of the atomic beam, so a non-zero transverse temperature of the atoms can contribute to the broadening. Furthermore, the geometry of the windows used to

perform these spectroscopy measurements does not allow for much control in the angle of incidence of the laser beam on the apparatus, so if the laser beam is not perfectly perpendicular to the direction of propagation of the atoms, part of the longitudinal velocity of the atoms could contribute to broadening the absorption line. In addiction to this, when the intensity of the incident light is sufficiently high, the rapidity of the excitation on an absorption transition can become greater than the rapidity of the relaxation. This leads to a considerable decrease in the number of atoms which are able to absorb the radiation (saturation) and represent a further contribution to the enlargement of the absorption line (saturation broadening, or power broadening). The enlargement due to the saturation effect is:

$$\gamma_s = \gamma\sqrt{1+S}$$

where γ_s is the saturated linewidth, γ is the natural linewidth of the transition and $S = \frac{I}{I_{sat}}$ is the saturation parameter. In our case the radius of the laser beam is about 1 mm for a power of 260 μW which corresponds to an average intensity of 8.2 $\frac{\text{mW}}{\text{mm}^2}$, and $S = 0.19$, which results in a saturated linewidth $\gamma_s \simeq 2\pi \times 35$ MHz, with a broadening of around 10%. We attribute the discrepancy with the experimental data to the residual Doppler broadenings discussed above, which, however, cannot be easily modeled.

6.2.4 Error signal

When the laser is left free to operate, its frequency exhibits slow drifts because of changing environmental conditions (e.g. temperature), and these fluctuations are undesirable in precision experiments. By stabilizing the master laser frequency to a stable external optical or atomic reference, it is possible to stabilize the frequency of the light that is emitted by the laser over time. For this purpose we reference the diode master laser to the atomic transition of strontium via a frequency modulation performed directly on the atomic beam [47]. In this way the frequency of light needed to excite such a transition is fixed by the properties of the reference atomic beam and is therefore very stable.

In order to generate a control signal, commonly called an error signal, which we can use to stabilize the frequency of our laser, we impose a modulation at a frequency of 250 kHz on the laser frequency. This modulation is applied directly to the current

driving the laser diode. An absorption signal generated with the modulated laser light is acquired through a photodiode and fed into a lock-in amplifier, which is already included into the laser driver. The signal is then demodulated at the same frequency as the laser modulation. The output signal of the lock-in amplifier serves as an error signal that is proportional to the first derivative of the absorption signal. Adding to the laser frequency ν_L a modulation of frequency ω and amplitude ε we obtain a frequency for the light incident on the sample:

$$\nu_L = \nu_L^0 \varepsilon \cos(\Omega t)$$

and the revealed signal can be written as:

$$S \simeq S_0 + L(\nu_L)$$

with S_0 background signal and $G(\nu_L)$ Lorentzian absorption.
If ε is small compared to the width of L we can develop the signal to first order thus obtaining:

$$S \simeq S_0 + L(\nu_L^0) + \left(\frac{dL}{d\nu}\right) \varepsilon \cos(\Omega t)$$

The absolute laser frequency can then be locked to the zero-crossing of the error signal providing a continuous restoring signal (feeding back on the laser current and/or the voltage of the extended-cavity piezoelectric transducer). that can be used to keep the laser frequency locked to the atomic transition reference.

While realizing the error signal, the choice of the intensity of the laser beam to be sent to the atoms is very important. In fact, when $I \ll I_{sat}$ the absorption is small so the error signal is low: in this regime it is better to increase the intensity in order to increase the signal height (which will not vary its width considerably). While when $I \gg I_{sat}$ the height of the signal is fixed by the saturation and will vary its width instead. In our case $250\,\mu$W is a reasonable compromise to have an absorption with a good signal-to-noise ratio, but without introducing significant power broadening, so as to have an error signal with an optimised slope. An example of an absorption spectrum and error signal is shown in figure 6.12. It was acquired with a laser power of $250\,\mu$W to ensure that we are below the saturation intensity and with the oven at a temperature of $440\,^\circ$C, which is the typical furnace operating temperature for conducting experiments.

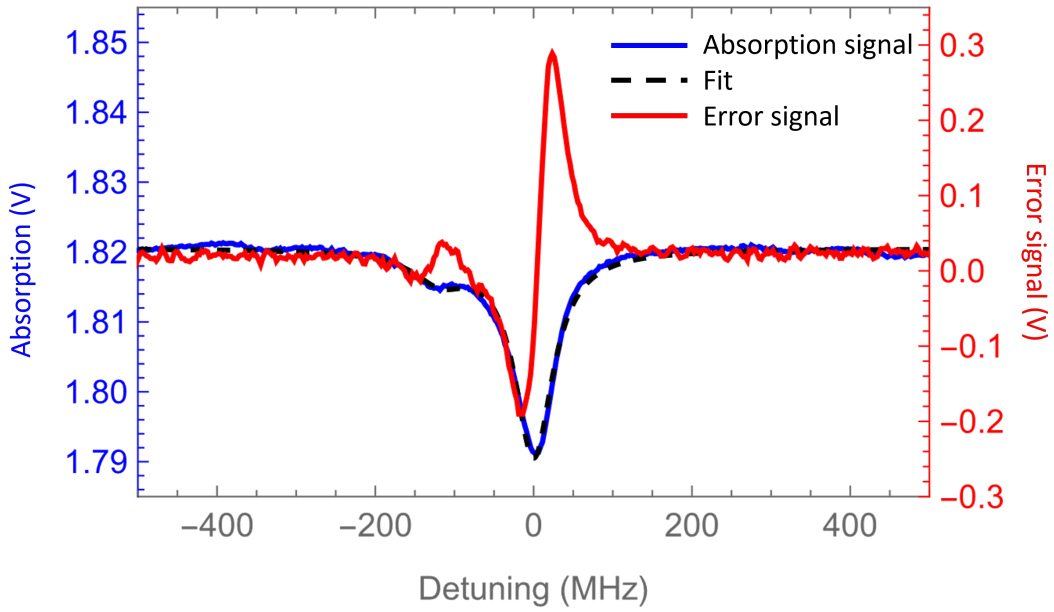

Figure 6.12: The blue line represents the absorption spectrum of the atoms probed with the master laser as a function of detuning to the ${}^1S_0 \rightarrow {}^1P_1$ transition performed with the oven at 440 °C. The black dotted curve shows the fit to the absorption spectrum and the red line is the error signal derived with frequency-modulation spectroscopy.

6.3 Red laser

The red laser employed in the experiment is a narrow linewidth, tunable CW Ti:Sapphire Laser by MSquared used to generate the 689 nm light. This laser has an output power of 3 W and wiil be used for the generation of the narrow-line 3D MOT ($\approx$ 200 mW), for one of the two photons needed for the excitation towards the Rydberg state ($\approx$ 2 W), for performing the Sysiphus cooling to the ground state in tweezer ($\approx$ 200 mW) and for its frequency stabilization with a high-finesse cavity ($\approx$ 1 mW).

In figure 6.13 I reported the measured $w(z)$ of the laser beam as a function

of the distance from the laser output windows, with the fit for a Gaussian beam propagation, as explained in section 6.1. The results of the fit are reported in the table 6.4.

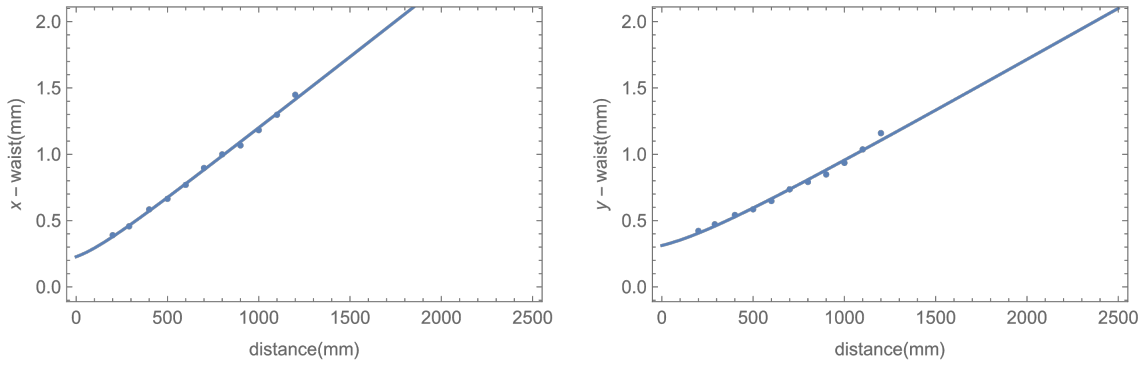

Figure 6.13: Measured w(z) along the transverse x and the y direction, as a function of the distance is taken from the laser output window. The line is a fit to equation 6.2.

	w_0 (mm)	waist z_0 (mm)
x-waist	0.203 ± 0.003	-95 ± 14
y-waist	0.282 ± 0.008	-173 ± 25

Table 6.4: Dimension and position of the waist of the red laser, the position value refers to the distance from the output window of the laser.

In order to obtain a beam size of about 0.5 mm in both the directions we use a telescope with two lenses of focal length $F = 30$ mm and $F = 50$ mm respectively, to increase the size of the the beam. These and all the setup built until now for the red laser are shown in figure 6.14. This laser is used to excite the ${}^1S_0 \rightarrow {}^3P_1$ transition of strontium which has a linewidth of 7.6 kHz. So we need a laser characterized by extremely pure spectral properties. To achieve this stable frequency we use a Pound-Drever-Hall stabilization technique with a high-finesse optical cavity realized in Ultra-Low Expansion (ULE) glass.

The laser beam is split into several parts through the use of variabile beam splitters obtained combining a half-wave plate with a polarizing beam spitter. The light used for the frequency stabilization passes trougth an acousto-optic modulator (AOM1), operating at 80 MHz, in double-passage configuration, and is then delivered inside the ULE via an optical fiber with an integrate electro-optical modulator (EOM). AOM1 is used to shift the laser frequency so that it is resonant on the

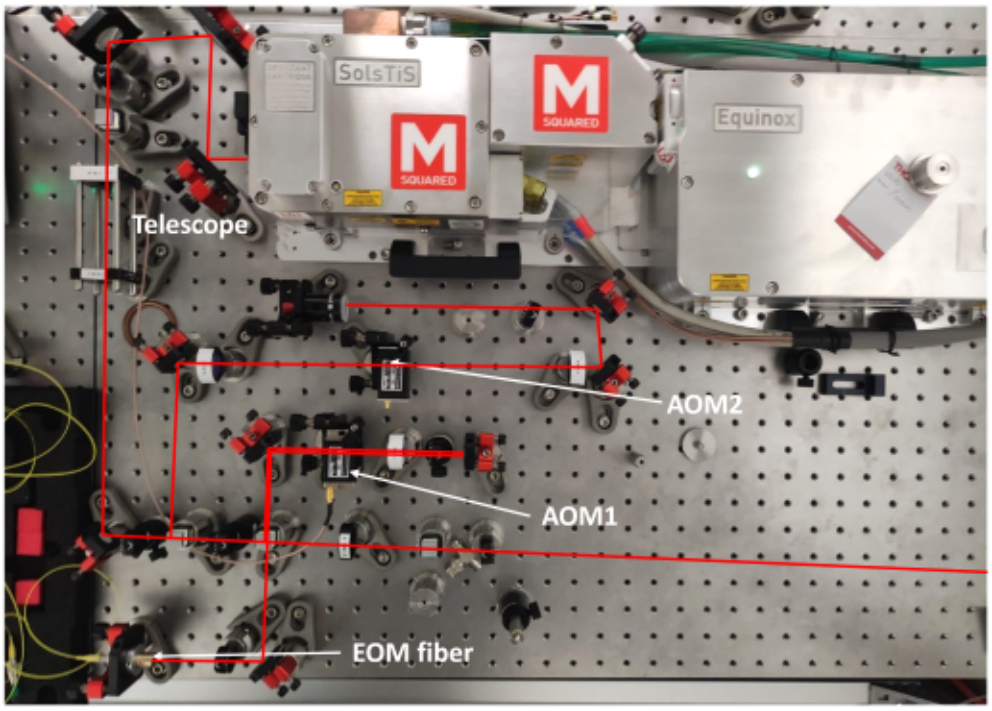

Figure 6.14: Picture of the optical setup for the red laser with all the main components.

cavity, while the EOM is used to apply the frequency modulation required for PDH coupling, which I will discuss later. The double passage in the AOM is performed with an efficiency of approximately 50 %, while the fiber coupling with an efficiency of about 18 %. The coupling efficiency is also particularly low because the fiber used has an insertion loss of 6 dB.

The optical cavity is illustrated in figure 6.15, is realized in Ultra-Low Expasion (ULE) glass with a finesse of about 300.000. The geometry of the cavity is studied so that it is minimally influenced by mechanical vibrations and the ULE glass is then chosen since its linear coefficient of thermal expansion (CTE) has a zero around room temperature to avoid thermal fluctuations, which would induce long term frequency drifts [49]. Being a plane-convex cavity, the waist of the foundamental cavity mode is located on the flat mirror of the cavity, 185 mm away from the cavity entrance in our case and it has a value of 209 μm. In order to realize a mode matching of

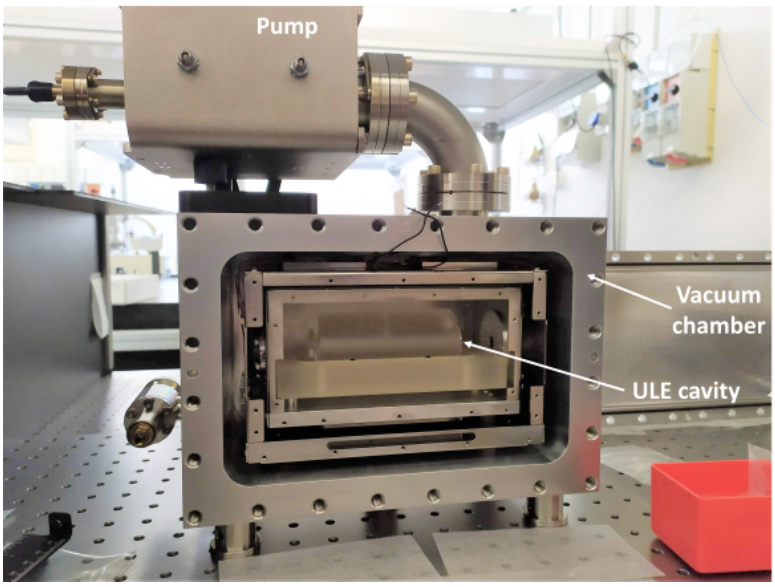

Figure 6.15: Picture of the ULE cavity inside the VH10500 vacuum chamber (Stable Laser Systems).

the laser beam with the cavity we need to use lenses arranged in the correct way to focus the waist of our laser beam in the same position as the waist of the cavity. In figure 6.16 the simulations carried out for a proper mode matching realization are shown. It should be noted that, since the beam is entering the cavity from the side of the spherical mirror, it is necessary to bear in mind that the presence of the latter is equivalent to having a lens with a focal length equal to half the radius of curvature of the mirror, thus $F = -250\,\mathrm{mm}$.

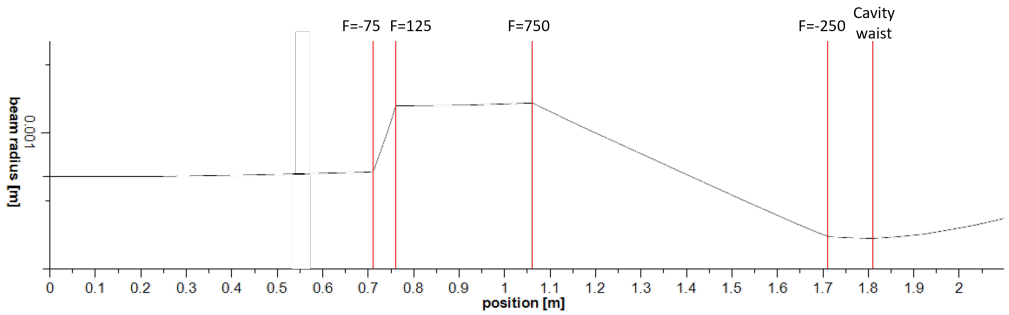

Figure 6.16: Simulation for the cavity mode-matching obtained from the software LaserCalc. The position are referred to the fiber output and the focal length are expressed in mm.

Using a telescope consisting of two lenses with focal lengths $F = -75\,\mathrm{mm}$ and

$F = 125\,\text{mm}$ and a lens with focal lengths $F = 750\,\text{mm}$ suitably positioned along the beam path, we achieve a cavity coupling with an efficiency of about 10%. The efficiency is not high and there may be room for improvement. However, it is not easy because of the geometrical constraints of the optical setup, which place limitations on the positioning of the lenses. In any case, the result can be considered satisfying since the power that will be needed for coupling to the cavity is very limited $(1, \text{mW})$, so I expect that the losses due to imperfect coupling will not significantly affect the total power budget.

The optimal mode-matching configuration for the set of lenses discussed before has been obtained experimentally by maximizing the coupling to the fundamental cavity mode. To this aim, the laser was kept scanning over a frequency range comprising one cavity free spectral range. We have first placed a CCD camera on the ouput mirror of the cavity and, while the laser was scanning, adjusted the position of the mode-matching lenses to observe the maximum intensity of the fundamental TEM00 cavity mode (the mode featuring no nodes in the transverse intensity profile), an example is shown in figure 6.17.

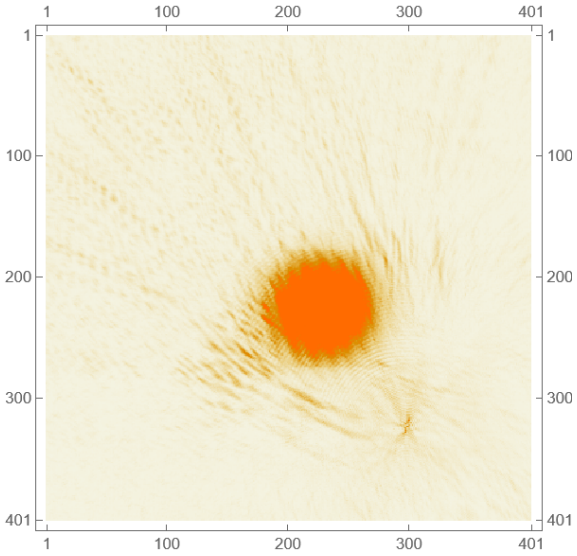

Figure 6.17: Picture of the fundamental TEM00 cavity mode obtained with a CCD camera placed on the ouput mirror of the cavity. The units on the horizontal and vertical axes are given in camera pixels, each pixel measuring $5.2\,\mu\text{m}$.

A finer adjustment was performed by replacing the CCD camera with a photodiode and optimizing the transmitted intensity signal.

6.3.1 Pound-Drever-Hall

The Pound–Drever–Hall (PDH) [50, 51] technique is a widely used and powerful approach for stabilizing the frequency of light emitted by a laser by means of locking to a stable reference. The idea behind the Pound-Drever-Hall technique is simple but powerful. If we have an accurate way to "measure" the laser frequency, then we can feed this measurement into the laser, with appropriate amplification and filtering, to hold the frequency (roughly) constant. One good way to measure the frequency of a laser beam is to send it into a Fabry–Perot cavity and look at the transmitted (or reflected) signal. Recall that light can only pass through a Fabry–Perot cavity if twice the length of the cavity is equal to an integer number of wavelengths of the light. So the frequency of the light wave must be an integer number times the cavity's free spectral range:

$$\Delta\nu_{\text{fsr}} = \frac{c}{2L}$$

where L is the length of the cavity and c is the speed of light. The cavity acts as a filter, with transmission lines, or resonances, spaced evenly in frequency every free spectral range. Figure 6.18 shows an example of the fraction of light transmitted through a Fabry–Perot cavity versus the frequency of the light.

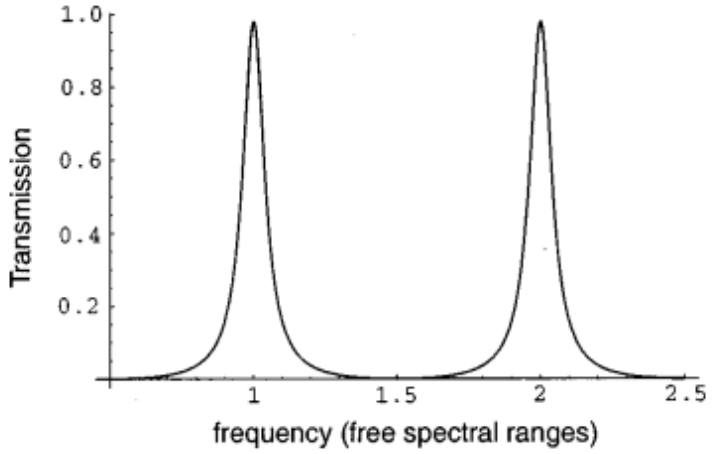

Figure 6.18: Transmission of a Fabry–Perot cavity vs frequency of the incident light. Int this theoretical example the cavity has a fairly low finesse, about 12, to make the structure of the transmission lines easy to see. Figure taken from [50].

If we were to operate just to one side of one of these resonances, but near enough that some light gets transmitted (say, half the maximum transmitted power), then

a small change in laser frequency would produce a proportional change in the transmitted intensity. We could then measure the transmitted intensity of the light and feed this signal back to the laser to hold this intensity (and hence the laser frequency) constant. The problem is that this way the system cannot distinguish between fluctuations in the laser frequency, which change the intensity transmitted through the cavity, and fluctuations in the intensity of the laser itself. A better method would be to measure the reflected intensity and hold that at a minimum, which would decouple intensity and frequency noise. The only problem with this scheme is that the intensity of the reflected beam is symmetric about resonance. If the laser frequency drifts out of resonance with the cavity, you can't tell just by looking at the reflected intensity whether the frequency needs to be increased or decreased to bring it back onto resonance. The derivative of the reflected intensity, however, is antisymmetric about resonance. If we were able to measure this derivative, we would have an error signal that we can use to lock the laser. Fortunately, this is not too hard to do: we can just vary the frequency a little bit and see how the reflected beam responds. Above resonance, the derivative of the reflected intensity with respect to laser frequency is positive. If we vary the laser frequency sinusoidally over a small range, then the reflected intensity will also vary sinusoidally, in phase with the variation in frequency. Below resonance, this derivative is negative. Here the reflected intensity will vary 180° out of phase from the frequency. On resonance the reflected intensity is at a minimum, and a small frequency variation will produce no change in the reflected intensity. By comparing the variation in the reflected intensity with the frequency variation we can tell which side of resonance we are on. Once we have a measure of the derivative of the reflected intensity with respect to frequency, we can feed this measurement back to the laser to hold it on resonance. The purpose of the Pound–Drever–Hall method is to do just this.

Figure 6.20 shows a sketch of our setup for the PDH locking while figure 6.19 shows a picture of the setup. First, it is necessary to modulate the phase of the incoming laser radiation to the cavity: this is done by using an EOM (which in our case is a fiber integrated electro-optical modulator), that we drive with a 30 MHz FR signal. The effect of this modulation is to generate three distinct frequency components, a carrier at the laser frequency and two sidebands at ±30 MHz. The experimental signal obtained by scanning the laser around the cavity resonance, the modulated laser light transmitted is acquired through a photodiode and converted

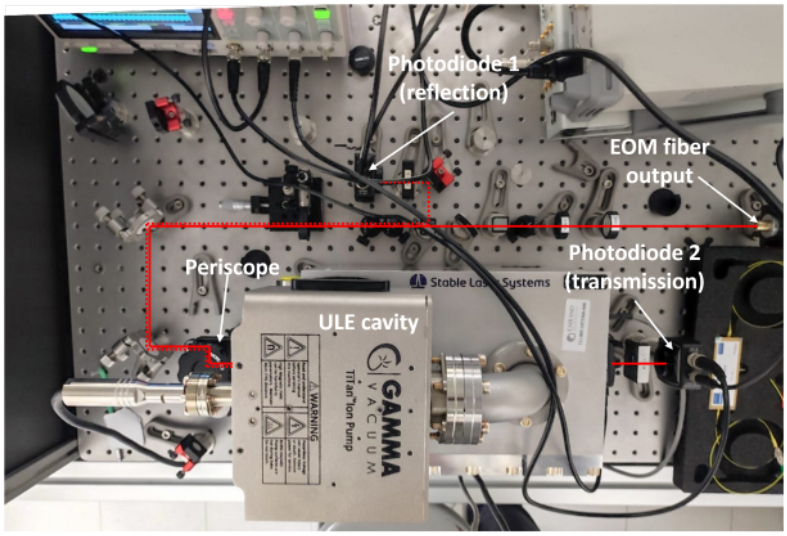

Figure 6.19: Picture of the optical setup for the Pound-Drever-Hall

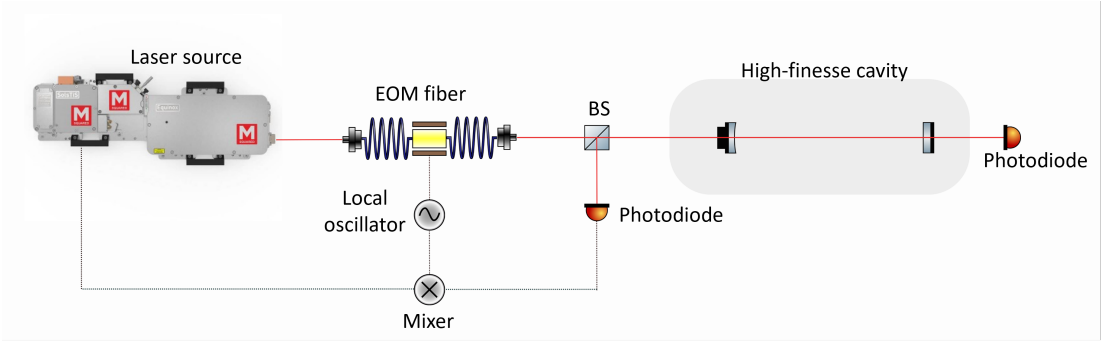

Figure 6.20: Schematic representation of the Pound-Drever-Hall lock loop.

into a voltage signal that is read on an oscilloscope is shown in figure 6.21.

Then, part of the intensity reflected from the cavity is picked up and sent to a photodiode. The generation of the PDH signal, explained above in the time domain, can be understood also in the frequency domain, from the interference of the sidebands in the light which is reflected from the cavity. We exemplify this description in the case of perfect mode-matching. In the case of perfect resonance with the cavity, the carrier frequency component is completely transmitted and the sidebands are reflected and sent to the photodiode. But if we are slightly out of resonance, part of the carrier is also reflected and, interfering with the light from the sidebands at the RF modulation frequency, whose phase depends on the detuning from the cavity. The intensity of the reflected light is analyzed with a fast

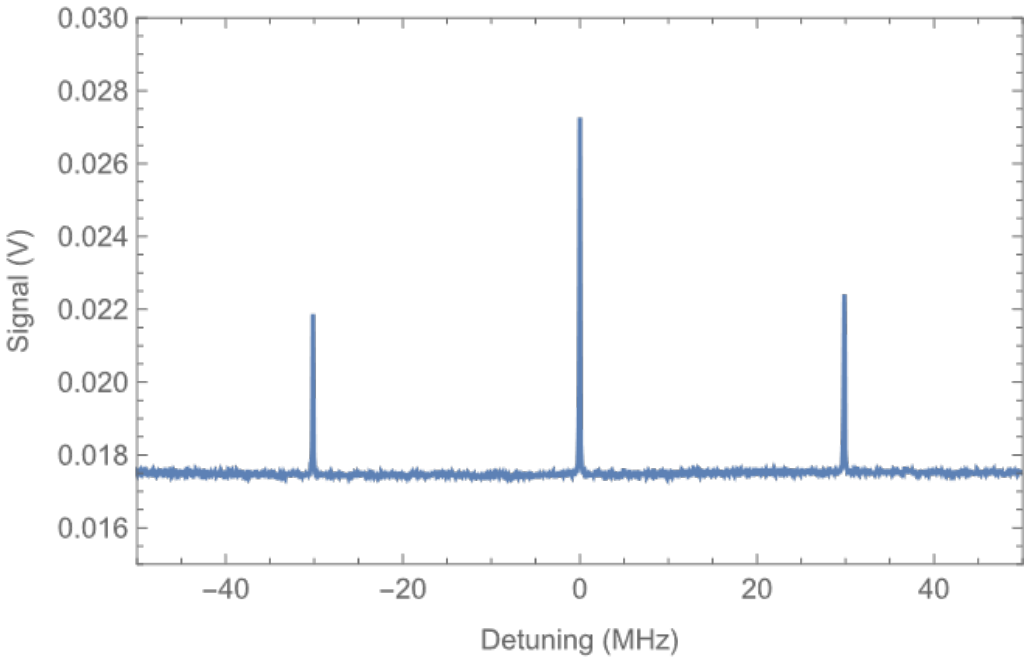

Figure 6.21: Experimental signal obtained by scanning the laser around the cavity resonance. The transmitted signal consists of a carrier and two sidebands at ± 30 MHz.

photodiode and the resunlting voltage is sent to a mixer together with the local oscillator signal at 30 MHz. The resulting signal is illustrated in figure 6.22. It is an antisymmetric signal around the resonance, positive if we are above resonance and negative if we are below. This signal, also called the error signal, is really the heart of this technique. Sending this signal back to an high voltage amplifier which drives a piezo mirror in the reference cavity of the Ti:Sa laser with a PI servo amplifier in a feedback loop would allow the frequency to be stabilized with extreme precision, and consequently would allow us to use the laser to excite the ultra-narrow $^1S_0 \rightarrow {}^3P_1$ transition of strontium.

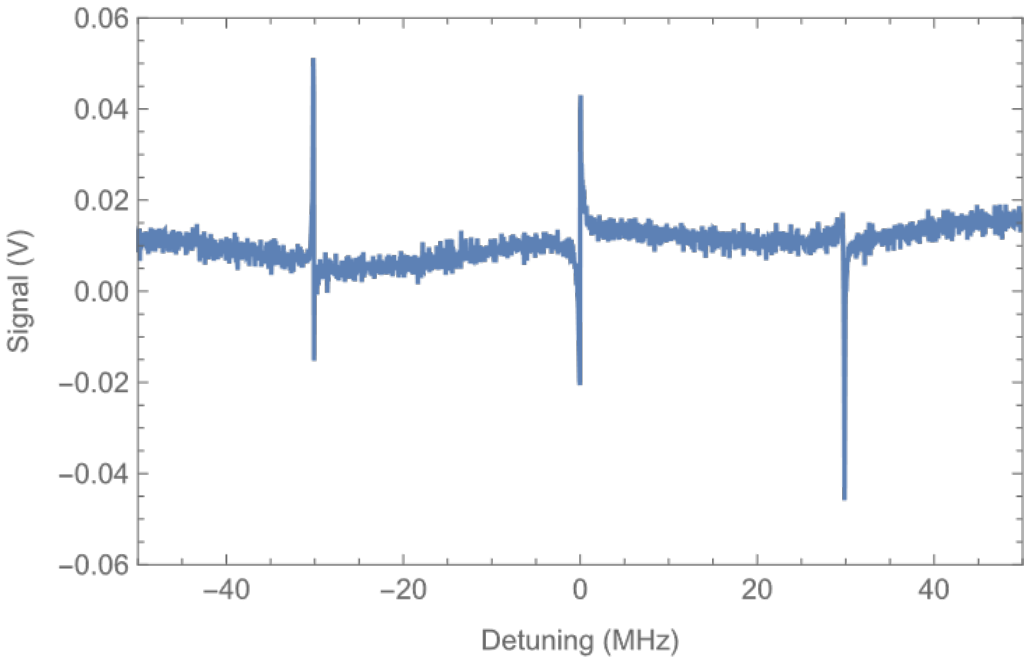

Figure 6.22: Experimental signal obtained by scanning the laser around the cavity resonance for the 689 nm laser. Dispersive signals centred around the carrier frequency component (central peak) and the two sidebands can be observed.

Chapter 7

Conclusions and perspectives

During the course of my thesis I worked on the development of the experimental setup for the realization of a novel quantum simulation platform based on strontium Rydberg atoms trapped in optical tweezers arrays. The studies carried out and the results reported in this thesis represent a fundamental step towards the completion of the first platform of this kind in Italy.

The simulations reported in chapter 5 allowed me to design a couple of high-field coils. These coils can produce really high magnetic fields (more than 900 G) to excite the Strontium clock transition on sub-ms timescales, allowing it to be used within experiments with tweezer atoms. In this way the clock state can be used as an intermediate state to realize strong single-photon excitation towards the Rydberg state and study magnetic models. Or it can be used as one of the two logical states of a qubit, together with the ground state, to realize fast quantum gates. These coils can also generate magnetic field gradients high enough to effectively trap atoms in MOTs, ensuring at the same time an effective cooling process of the coils. Dissipating the heat generated by the Joule effect from the current flowing in the coils is essential to prevent damage to the experimental apparatus, but also so that the increase in temperature does not interfere with the performance of the experiment. Based on the results of these simulations, the high-field coils were commissioned to the OSWALD company and will be delivered in the coming months, together with all the equipment required for their operation as power supply and chillers.

The study of the laser sources and of the atomic source I have performed and then reported in chapter 6 is also fundamental in the realization of the apparatus. The blue laser operating on the broad transition $^1S_0 \rightarrow {}^1P_1$ at 461 nm will be directly

referenced on the atomic transition of strontium via the spectroscopy setup I have designed and used to characterized the atomic flux. Instead the red laser operating on the narrow transition ${}^1S_0 \rightarrow {}^3P_1$ at 689 nm, which is 7.6 kHz wide, requires a better frequency stabilization, and this will be achieved with the PDH setup on the high-finesse ULE cavity that I have designed and assembled during the thesis.

The development of the platform will continue in the coming months, and the next steps will be the realization and characterization of the two MOTs that will exploit both the coils and the frequency-stabilized lasers studied in this thesis. Then it will be necessary to study and optimize the generation and rearrangement process of the array of atoms trapped in the tweezers, together with the detection and excitation scheme to the Rydberg state.

Once completed, this platform is expected to guarantee a high degree of control over individual atoms in terms of both their position and their internal state, together with the possibility to upscale the number of atoms in the array quite easily. This will make this apparatus really suitable for advanced quantum simulations of quantum spin models and for the realization and study of quantum gates with qubits generated by exploiting controlled entanglement between atoms through the Rydberg blockade mechanism.

Bibliography

[1] Iulia Buluta and Franco Nori, Quantum simulators, Science **326**,108 2009.

[2] R. Feynman, Simulating Physics with Computers, Int. J. Theor. Phys. **21**, 467 (1982).

[3] E. Altman et al., Quantum Simulators: Architectures and Opportunities, PRX Quantum **2**, 017003 (2021).

[4] Aspuru-Guzik and P. Walther, Photonic quantum simulators. Nature Phys. **8**, 285291 (2012).

[5] R. Blatt and C. Roos, Quantum simulations with trapped ions, Nature Phys. **8**, 277284 (2012)

[6] C. Gross and I. Bloch, Quantum simulations with ultracold atoms in optical lattices, Science **357**, 9951001 (2017).

[7] P. Barthelemy and L.M.K. Vandersypen, , Quantum Dot Systems: a versatile platform for quantum simulations, ANNALEN DER PHYSIK **525**, 808826 (2013).

[8] A. Browaeys and T. Lahaye, Many-body physics with individually controlled Rydberg atoms, Nat. Phys. **16**, 132142 (2020).

[9] H. Bernien, et al., Probing many-body dynamics on a 51-atom quantum simulator, Nature **551**, 579584 (2017).

[10] Levine H. et al., Quantum phases of matter on a 256-atom programmable quantum simulator, Nature Physics **595**, 227232 (2021).

[11] G. Semeghini et al., Probing topological spin liquids on a programmable quantum simulator, Science **374**, 6572 (2021).

[12] C. Alexandre et al,. Alkaline-earth atoms in optical tweezers, Phys. Rev. X **8**, 041055 (2018).

[13] J. Wilson et al., Trapped arrays of alkaline earth rydberg atoms in optical tweezers, Phys. Rev. Lett, **128**, 033201 (2022).

[14] https://physics.nist.gov/PhysRefData/Handbook/Tables/strontiumtable1.htm

[15] I. Madjarov, Entangling, controlling, and detecting individual strontium atoms in optical tweezer arrays. PhD thesis, California Institute of Technology, Pasadena, California, (2021).

[16] I. Madjarov et al., An atomic-array optical clock with single-atom readout, Physical Review X **9**, 041052 (2019).

[17] M. Schioppo et al., Ultrastable optical clock with two cold-atom ensembles. Nature Photonics **11**, 48–52 (2017).

[18] A. Taichenachev et al, Magnetic Field-Induced Spectroscopy of Forbidden Optical Transitions with Application to Lattice-Based Optical Atomic Clocks, Physical Review Letters **96**, 083001 (2006).

[19] H. Levine et al., Parallel implementation of high-fidelity multiqubit gates with neutral atoms, Phys. Rev. Lett. **123**, 170503 (2019).

[20] T. F. Gallagher, Rydberg Atoms, Cambridge Univ. Press (1994).

[21] N. Sibalić and C.S. Adams, Rydberg Physics, IOP (2018).

[22] C. Roos et al., Designer atoms for quantum metrology, Nature **443**, 316319 (2006).

[23] R. Grimm, M. Weidemüller and Y.B. Ovchinnikov, Optical dipole traps for neutral atoms, Advances in Atomic, Molecular and Optical Physics Vol. 42, 95-170 (2000).

[24] N. Schlosser, G. Reymond, and P. Grangier, Collisional Blockade in Microscopic Optical Dipole Traps, Phys. Rev. Lett. **89**, 023005 (2002).

[25] A. Fuhrmanek, R. Bourgain, Y. R. P. Sortais, and A. Browaeys. Light-assisted collisions between a few cold atoms in a microscopic dipole trap. Phys. Rev. A **85**, 062708 (2012).

[26] D. Barredo et al., An atom-by-atom assembler of defect-free arbitrary two-dimensional atomic arrays, Science **354**, 10211023 (2016).

[27] F. Robicheaux and J. V. Hernandez. Many-body wave function in a dipole blockade configuration. Phys. Rev. A **72**, 063403 (2005).

[28] W. D. Phillips, Nobel Lecture: Laser cooling and trapping of neutral atoms, RevModPhys.70. 721, (1998).

[29] W. D. Phillips and H. Metcalf, Laser deceleration of an atomic beam. Physical Review Letters **48**, 596 (1982).

[30] T. W. Hänsch and A. L. Schawlow, Cooling of gases by laser radiation. Opt. Commun. **13**, 6869 (1975).

[31] A. Baumgärtner. A new apparatus for trapping and manipulating single Strontium atoms. Master thesis, California Institute of Technology, Pasadena, California, (2017).

[32] Y. Castin, H. Wallis, and J. Dalibard. Limit of doppler cooling. JOSA B, **6**, 20462057 (1989).

[33] V. V. Ivanov and S. Gupta, Laser-Driven Sisyphus Cooling in an Optical Dipole Trap, Phys. Rev. A **84**, 063417 (2011).

[34] A. M. Kaufman, B. J. Lester, and C. A. Regal, Cooling a Single Atom in an Optical Tweezer to Its Quantum Ground State, Phys. Rev. X **2**, 041014 (2012).

[35] AC/DC Module User's guide, COMSOL 5.4.

[36] Bruce R. Munson, Theodore H. Okiishi, Wade W. Huebsch, Alric P. Rothmayer, Fundamentals of Fluid Mechanics, 7th edition.

[37] John W. Mitchell, Fox and McDonald's introduction to fluid mechanics ,University of Wisconsin-Madison, 10th edition. Wiley, (2020).

[38] CFD Module User's guide, COMSOL 5.4.

[39] R. Shankar Subramanian, Heat transfer in Flow Through Conduits. Department of Chemical and Biomolecular Engineering Clarkson University.

[40] Chia-Ch'iao Lin. Turbulent Flows and Heat Transfer. ISBN: 9780691652528. Princeton University Press (1959).

[41] http://pcfarina.eng.unipr.it/dispense98/Dieci113704/Dieci113704.htm. Notes on heat exchange, Angelo Farina, University of Parma.

[42] K.S. Hardman, S. Bennetts, J.E. Debs, C.C.N. Kuhn, G.D. McDonald, N. Robins, JoVE **86**, e51184 (2014).

[43] C. J. Buczek, R. J. Freiberg and M. L. Skolnick, Laser injection locking, IEEE, 14111431 (1973).

[44] S. Stellmer, Degenerate quantum gases of strontium. PhD thesis, Faculty of Mathematics, Computer Science and Physics of the University of Innsbruck, (2013).

[45] H. Pauly, Atom, Molecule, and Cluster Beams I: Cluster Beams, Fast and Slow Beams, Accessory Equipment and Applications (Springer Science & Business Media, 2000),Vol. 1.

[46] T, Yang et al. A high flux source of cold strontium atoms. Eur. Phys. J. D **69**, 226 (2015).

[47] W. Jitschin, Locking the laser frequency to an atomic transition, Appl. Phys. B **33**, 7–8 (1984).

[48] O. Svelto. Principles of Lasers. Springer US, (2010).

[49] S. A. Webster, M. Oxborrow, S. Pugla, J. Millo, and P. Gill. Thermal-noise limited optical cavity. Phys. Rev. A **77**, 033847 (2008).

[50] E. D. Black. An introduction to Pound-Drever-Hall laser frequency stabilization. Am. J. Phys. **69**, (2001).

[51] R. V. P. Drever et al., Laser phase and frequency stabilization using an optical resonator. Appl. Phys. B **31**, 97105 (1983).

Acknowledgment

At the end of this journey, it is only right for me to extend my heartfelt thanks to the people who have been with me.

First of all, I would like to thank Leonardo Fallani for getting me interested in this field right from the ultra-cold atoms course. Following his lectures I decided what I wanted to do "when I grew up". Thank you for following me over these months and during the writing of this thesis with infinite patience.

Here I also wanted to thank Giacomo Cappellini for constantly following my workand teaching me so many things over the last few months, especially how to work in the lab.

Special thanks also goes to Luca Guariento, Vladislav Gavryusev and Jacopo Catani for putting up with me during these months. Thank you all for making me feel from the very first day part of a team of amazing people, where I was able to work and grow a lot while also having fun.

I would also like to thank my family, which has been by my side throughout my university career, supporting me immensely. I firmly believe that on more than one occasion my mother was much more convinced than I was about what my path and my successes would be.

Thanks to my lifelong friends who are a constant, you were always there at the most important moments, I cannot even describe how grateful I feel to have you by my side.

Thanks to my university mates, with whom I have shared moments of ups and downs in these years and who have become a second family for me. They are probably the real victims of this thesis, forced to suffer all my anxieties and fears and who have often given me the strength to go on, because discomfort is less if it is shared.